Neuron

Article

The Dentate Gyrus Classifies Cortical Representations of Learned Stimuli

Highlights

- Odor identities are represented in the population activity of DG GCs
- Synaptic input from LEC is required for odor coding in DG GCs
- Odor classification accuracy in DG is correlated with behavioral discrimination
- Learning modifies odor representations in DG GCs

Authors

Nicholas I. Woods, Fabio Stefanini, Daniel L. Apodaca-Montano, Isabelle M.C. Tan, Jeremy S. Biane, Mazen A. Kheirbek

Correspondence

mazen.kheirbek@ucsf.edu

In Brief

Animals use cues in their environments to guide behavior and, with experience, modify internal representations of these cues to guide future behavior. Woods, Stefanini, et al. use high-resolution calcium imaging to show that dentate gyrus granule cells encode and discriminate olfactory information and these representations are enhanced by associative learning.

Woods et al., 2020, Neuron *107*, 173–184
July 8, 2020
https://doi.org/10.1016/j.neuron.2020.04.002

CellPress

Neuron

CellPress

Article

The Dentate Gyrus Classifies Cortical Representations of Learned Stimuli

Nicholas I. Woods,[1,2,8] Fabio Stefanini,[3,8] Daniel L. Apodaca-Montano,[4] Isabelle M.C. Tan,[4] Jeremy S. Biane,[4] and Mazen A. Kheirbek[1,4,5,6,7,9,*]

[1]Neuroscience Graduate Program, University of California, San Francisco, San Francisco, CA 94158, USA
[2]Medical Scientist Training Program, University of California, San Francisco, San Francisco, CA 94158, USA
[3]Center for Theoretical Neuroscience, Mortimer B. Zuckerman Mind Brain Behavior Institute, Department of Neuroscience, Columbia University, New York, NY 10027, USA
[4]Department of Psychiatry, University of California, San Francisco, San Francisco, CA 94158, USA
[5]Kavli Institute for Fundamental Neuroscience, University of California, San Francisco, San Francisco, CA 94158, USA
[6]Weill Institute for Neurosciences, University of California, San Francisco, San Francisco, CA 94158, USA
[7]Center for Integrative Neuroscience, University of California, San Francisco, San Francisco, CA 94158, USA
[8]These authors contributed equally
[9]Lead Contact
*Correspondence: mazen.kheirbek@ucsf.edu
https://doi.org/10.1016/j.neuron.2020.04.002

SUMMARY

Animals must discern important stimuli and place them onto their cognitive map of their environment. The neocortex conveys general representations of sensory events to the hippocampus, and the hippocampus is thought to classify and sharpen the distinctions between these events. We recorded populations of dentate gyrus granule cells (DG GCs) and lateral entorhinal cortex (LEC) neurons across days to understand how sensory representations are modified by experience. We found representations of odors in DG GCs that required synaptic input from the LEC. Odor classification accuracy in DG GCs correlated with future behavioral discrimination. In associative learning, DG GCs, more so than LEC neurons, changed their responses to odor stimuli, increasing the distance in neural representations between stimuli, responding more to the conditioned and less to the unconditioned odorant. Thus, with learning, DG GCs amplify the decodability of cortical representations of important stimuli, which may facilitate information storage to guide behavior.

INTRODUCTION

Animals have a cognitive map of their surroundings that is constantly updated to optimize behavior (McNaughton et al., 2006; Olton et al., 1979). Any given element of their surroundings may not carry immediate meaning, but with reinforcement, animals will learn to approach or avoid cues that predict salient outcomes and ignore others. One way that neural populations may implement this form of encoding is by increasing the distance between neural representations of cues through the process of learning, effectively "separating" a salient from a non-salient stimulus.

One potential locus of this computation may be the hippocampus (HPC), which not only contributes to spatial navigation and memory (Eichenbaum et al., 2007; Olton et al., 1979; Tulving and Markowitsch, 1998) but also encodes non-spatial stimuli and the relationship between these behaviorally relevant variables (Aronov et al., 2017; Igarashi et al., 2014; Li et al., 2017; MacDonald et al., 2013; Martin et al., 2007). However, how experience can impact the representations of non-spatial stimuli in the HPC has remained largely unexplored. Here, we turned to olfactory stimuli to investigate how dentate gyrus granule cells (DG GCs) encode and separate incoming sensory information. Early anatomists noted the extensive connectivity and proximate location of the hippocampus with other parts of the olfactory system and accordingly included the hippocampus as a central node in the rhinencephalon or "nose brain" (Broca, 1878; Eichenbaum and Otto, 1992). Subsequent electrophysiological studies revealed that odorants were uniquely capable as sensory stimuli in eliciting a burst of activity in the DG; however, technical constraints limited a more complete understanding of how the DG encodes and processes this information (Vanderwolf, 1992; Wilson and Steward, 1978). Extensive work has elucidated how olfactory information is represented at initial sensory-processing centers, such as the olfactory bulb and piriform cortex (Bathellier et al., 2008; Bolding and Franks, 2017; Iurilli and Datta, 2017; Meister and Bonhoeffer, 2001; Roland et al., 2017; Sosulski et al., 2011; Stettler and Axel, 2009; Uchida and Mainen, 2003; Xu and Wilson, 2012), yet little is known of the logic by which odorant stimuli are represented or learned within the DG.

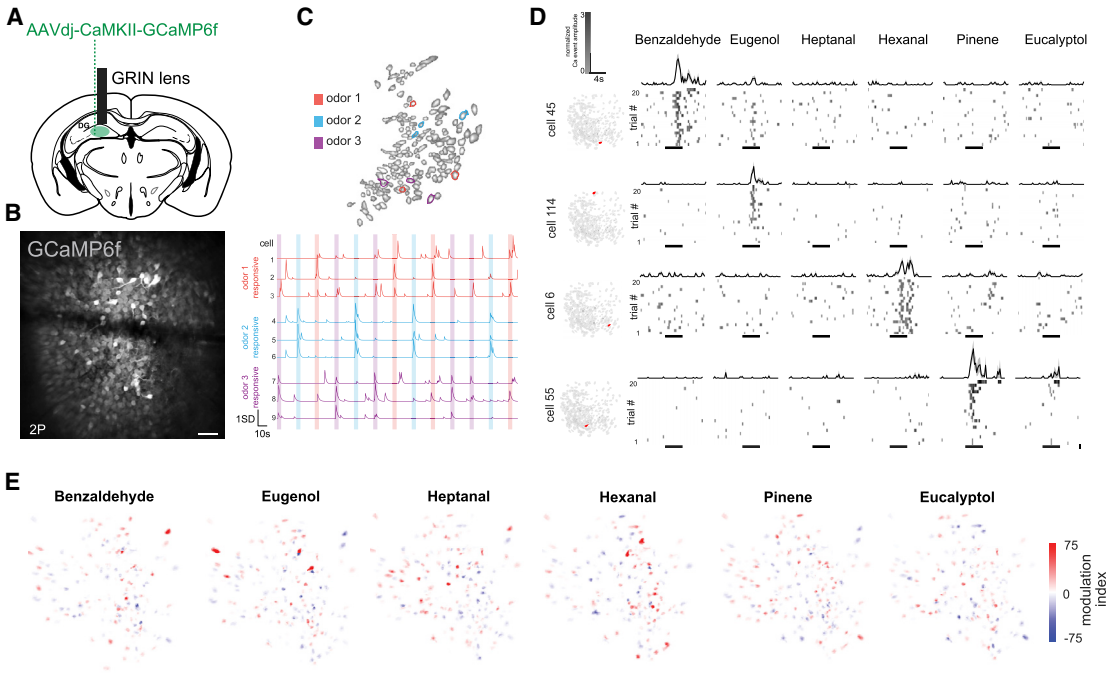

Figure 1. Odor Responses in DG GCs

(A) Experimental design. GCaMP6f is expressed in DG GCs for two-photon microscopy imaging of odor responses in DG GCs in awake-behaving mice.

(B) Standard deviation projection of *in vivo* two-photon image from a representative DG FOV. Scale bar: 50 μm.

(C) Odor-evoked neural responses in 9 example DG GCs, spatial footprints of identified ROIs on left, with denoised calcium traces on right (odor delivery periods indicated with shading).

(D) Normalized calcium events and cell maps from DG GC FOVs. Example cell responses during exposure to a six-odor panel (20 trials). Normalized Ca event magnitude was generated by dividing each event magnitude by the mean event magnitude across the session and averaged across trials. 4-s odor delivery times noted below raster, with average responses above trace (mean [black] plus SEM [gray]).

(E) Odor responses are sparse and randomly distributed in the FOV. Spatial footprints shown are from an example mouse, with modulation index for each cell (see STAR Methods).

Anatomical studies suggest odor-related information is transmitted to the DG via inputs from the lateral entorhinal cortex (LEC) (Eichenbaum et al., 2007; Hargreaves et al., 2005; Leitner et al., 2016; Witter et al., 2017), which itself receives olfactory inputs via both direct projections from the olfactory bulb and afferents originating in the piriform cortex and cortical amygdala (Heale and Vanderwolf, 1994, 1999; Krettek and Price, 1977; Leitner et al., 2016; Room et al., 1984; Shipley and Adamek, 1984; Vanderwolf, 1992; Wilson and Steward, 1978). In addition, the DG has been hypothesized to disambiguate cortical representation of sensory stimuli, so as to create less or non-overlapping outputs to the downstream CA3 subfield of the HPC (Aimone et al., 2011; Knierim and Neunuebel, 2016; Yassa and Stark, 2011). However, how learning impacts this process, and whether olfactory representations are separated at the level of DG neural activity, remains largely unknown.

In order to understand how the DG classifies cortical representations of salient olfactory stimuli, we performed *in vivo* chronic two-photon imaging of the LEC and DG. We investigated (1) how DG GCs and LEC neurons represent olfactory stimuli, (2) whether LEC is the main input for olfactory information to DG, and (3) how DG GCs and LEC neurons change their responses with learning. We found that odor identity is robustly represented in the DG and that the degree to which the DG classified odorants was directly related to discrimination of these cues during context recall. Odors were more accurately classified in populations of cells within the DG than LEC, and with learning, the DG GCs flexibly changed their representations of odor stimuli more so than LEC neurons, increasing the distance in neural representation between stimuli and responding more to the conditioned odorant. These data reveal that DG GCs may be a part of an extended network that represents the olfactory world and are involved in learning the associations between olfactory stimuli and behaviorally relevant outcomes.

RESULTS

Representations of Olfactory Stimuli in LEC and DG

To determine whether odor information is represented in the DG, we performed chronic high-resolution, two-photon calcium imaging of DG GCs in awake, head-fixed mice (Danielson et al., 2016). We visualized GC activity by injecting an adeno-associated virus (AAV) expressing GCaMP6f into the DG and imaged fields of view (FOVs) within the DG granule cell layer (GCL) (Figures 1A and 1B; Video S1). To characterize baseline responses to odorants, mice were imaged during delivery of a panel of diverse monomolecular odorants (Figure 1A). Olfactory stimuli evoked robust responses in a fraction of GCs (Figures 1C,

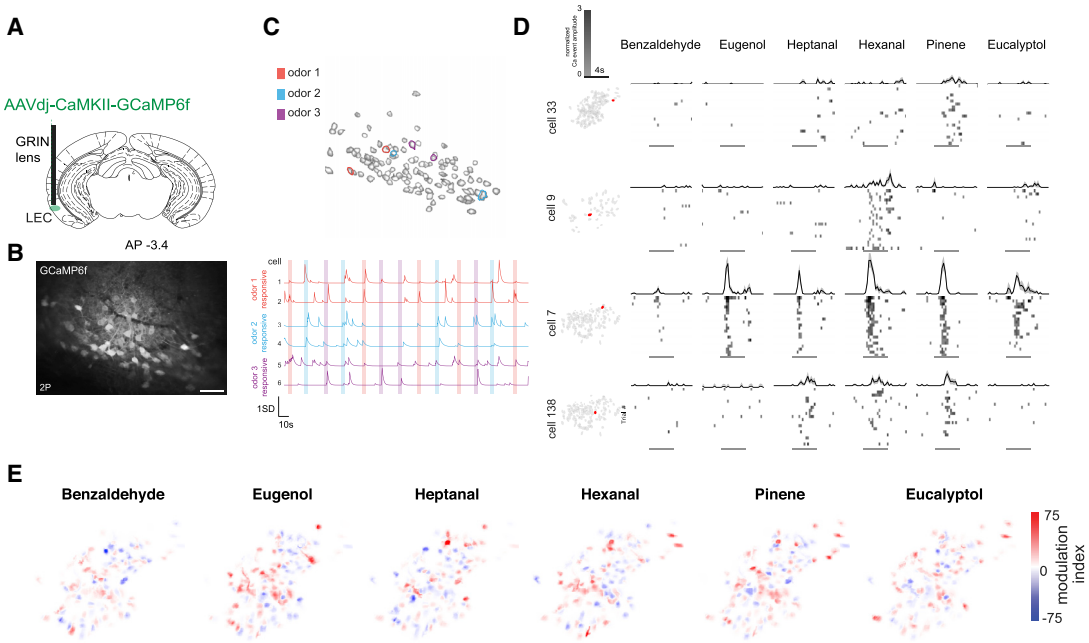

Figure 2. Odor Responses in LEC

(A) Experimental design. GCaMP6f is expressed in LEC neurons for two-photon microscopy imaging of odor responses in awake-behaving mice.

(B) Standard deviation projection of *in vivo* two-photon image from a representative LEC FOV. Scale bar: 50 μm.

(C) Odor-evoked neural responses in 9 example LEC neurons, spatial footprints of identified ROIs on left, with denoised calcium traces on right (odor delivery periods indicated with shading).

(D) Normalized calcium events and cell maps from LEC FOVs. Example cell responses during exposure to a six-odor panel (20 trials). Normalized Ca event magnitude was generated by dividing each event magnitude by the mean event magnitude across the session and averaged across trials. 4-s odor delivery times are noted below raster, with average responses above trace (mean [black] plus SEM [gray]).

(E) Odor responses are sparse and randomly distributed in the FOV. Spatial footprints shown are from an example mouse, with modulation index for each cell (see STAR Methods).

S1D, S1G, S2B, and S2C) that remained stable across multiple trials (Figure 1D). As is also the case for odor-evoked responses in upstream piriform cortex (Roland et al., 2017; Stettler and Axel, 2009), which innervates LEC (Heale and Vanderwolf, 1994, 1999; Krettek and Price, 1977; Leitner et al., 2016; Room et al., 1984; Shipley and Adamek, 1984; Vanderwolf, 1992; Wilson and Steward, 1978), odor-modulated GCs were distributed across the FOV without apparent spatial clustering (Figures 1E, S1F, and S2A). In order to understand how odor information may be differentially represented in the DG and its upstream input, LEC, we developed a method for two-photon imaging of GCaMP6f-expressing LEC neurons in awake, head-fixed mice (Figure 2B; Video S2). As in DG, a subset of LEC neurons showed time-locked responses to odor delivery, with no discernable spatial clustering of modulated cells (Figures 2A–2C, S1E, S2B, and S2C).

We next sought to compare odor responses in LEC neurons, DG GCs, and DG GCs in which input from LEC was inhibited. In our six-odor delivery design, we imaged DG GCs, LEC neurons, and DG GCs from mice in which we silenced LEC-DG synaptic transmission bilaterally using tetanus toxin light chain (LEC-DG TeLC) (see STAR Methods; Figures 3A and S1C). The identity of presented odorants could be accurately decoded using linear decoders (Bishop, 2006) from the population activity of DG GCs and LEC neurons, but not from LEC-DG TeLC mice (Figures 3B, 3C, and S2D–S2F; see STAR Methods), suggesting the LEC is the major source of odor input to the DG. By comparing decoding accuracies in LEC and DG, we found that a decoder trained on DG GC data could more accurately classify odor identity than one trained on LEC activities, suggesting that odor identity is more reliably represented in DG than LEC (Figure 3C). This was true both in experiments using a six-odor panel and a three-odor panel (Figures S2D and S2E). We obtained complementary results by constructing population vectors of DG GCs or LEC activity during odor presentations and measuring trial by trial similarity; we found responses across odors were less correlated in DG when compared to LEC (Figures 3E, S2G, and S2H), indicating that distinct odor representations are decorrelated in DG compared to LEC and that odor correlations were disrupted in LEC-DG TeLC mice (Figure 3E). Finally, we constructed a model based on random connectivity (Schaffer et al., 2018) between LEC and the target GCs (see STAR Methods) to determine whether this could recapitulate the high decoding accuracy in DG GCs seen in our data. The property of random connectivity in the model maintained correlations in odor representations within the input structure (LEC) and enabled expansion of the dimensionality of patterns onto its output structure (DG) via a non-linear transformation, which in general can be beneficial for decoding (Barak et al.,

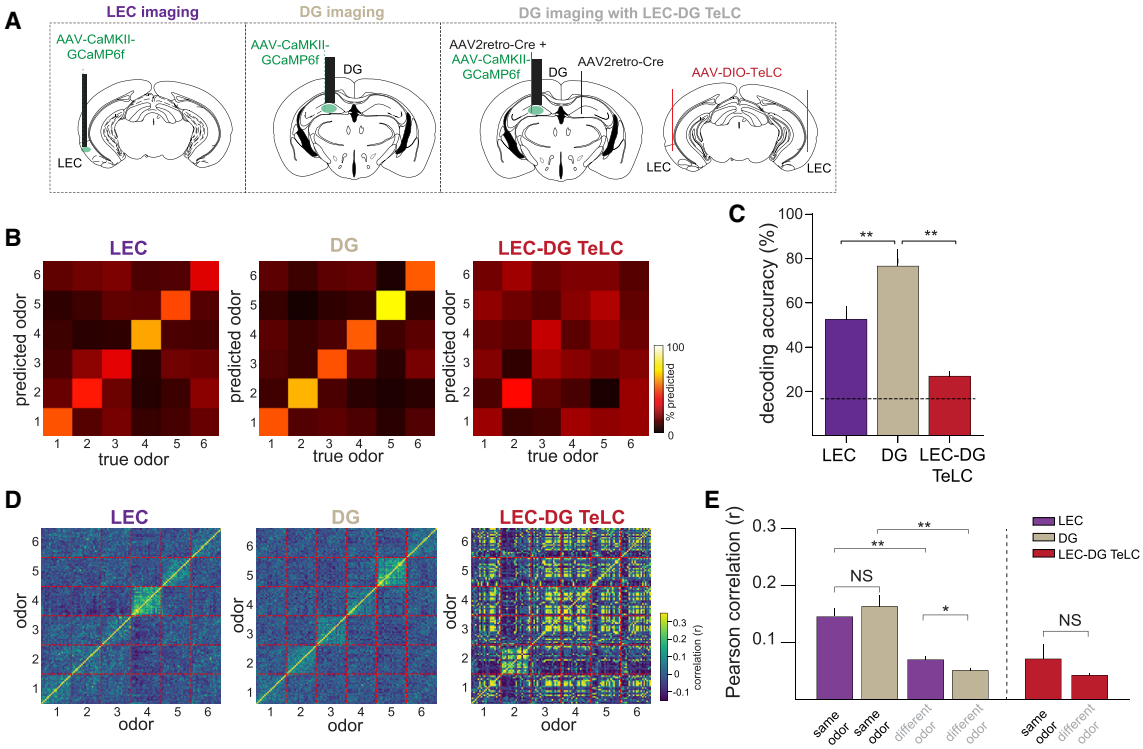

Figure 3. Neural Representations of Olfactory Stimuli in DG, LEC, and LEC-DG TeLC Mice

(A) Experimental cohorts for imaging DG, LEC, and the DG of LEC-DG TeLC mice (see STAR Methods).

(B) Confusion matrix for decoding of six odors (1, benzaldehyde; 2, eugenol; 3, heptanal; 4, hexanal; 5, pinene; 6, eucalyptol) from LEC neurons, DG GCs, and DG GCs from LEC-DG TeLC mice.

(C) Quantification of odor decoding accuracies. Odor decoding accuracy was significantly better in DG GCs than LEC neurons, and decoding accuracy was significantly reduced in LEC-DG TeLC DG GCs (linear support-vector machine [SVM] classifier with matched number of cells in DG, LEC, and LEC-DG TeLC mice n = 189 cells [n-matched] from 8 DG, 7 LEC, and 3 LEC-DG TeLC mice; Mann-Whitney U test; $^{**}p < 0.01$).

(D) Trial-by-trial similarity matrix for same six odors as in (B) from recordings of LEC neurons, DG GCs, and DG GCs from LEC-DG TeLC mice.

(E) Quantification of Pearson correlation coefficients revealed lower across odor correlations in DG GCs as compared to LEC neurons.

No significant difference was found between, within, and across odor correlations in DG GCs from LEC-DG TeLC mice; n = 8 DG, 7 LEC, and 3 LEC-DG TeLC mice; t test; $^{*}p < 0.05$; $^{**}p < 0.01$. Error bars represent ± SEM. For exact p values, see Table S1.

2013). However, random connectivity alone, at all tested DG sparsity levels in our model, was not sufficient to obtain the high decoding performance we observed in our DG recordings, using either the six-odor panel or the three-odor panel (Figures S2G and S2H). These data suggest that LEC input to DG is required for odor classification and that local circuit operations within the DG itself may enhance odor representations rather than arising solely from random connectivity between LEC and DG.

Odor Classification Accuracy in the DG Is Related to Behavioral Discrimination in an Odor-Guided Contextual Memory Task

We next asked whether odor coding in the DG was related to the discrimination of odors when used as cues for contextual recall. In DG-dependent contextual fear discrimination/generalization experiments, a main cue used to distinguish contexts is the ambient odor cue present in each context (Danielson et al., 2016; McHugh et al., 2007; Sahay et al., 2011). We thus asked whether the accuracy of odor classification in the DG was related to use of these cues for contextual recall. To test this, we developed an odor-guided contextual fear memory task where mice discriminated contexts that differed in the ambient odor present. We used two chemically similar odorants, ethyl butyrate (EB) and methyl butyrate (MB), and one distinct odorant, isoamyl acetate (IAA). On day 1, mice explored the three contexts in order to assess baseline levels of freezing. The next day, mice received mild footshocks in a novel context (context d) infused with the MB odor from context b and, finally on day 3, were re-exposed to the three pre-training contexts and tested for freezing in three contexts (Figure 4A). Compared to control mice, LEC-DG TeLC mice showed lower levels of freezing in the context infused with the odor present during conditioning and did not differ in freezing levels across contexts (Figure 4A). This suggests that LEC-DG TeLC mice did not use the odor as a cue for memory recall of the conditioned context. This was consistent with a role for the DG in context encoding and for the LEC in integrating contextual representations with non-spatial stimulus representations (Basu et al., 2016; Danielson et al., 2016; Hargreaves et al., 2005; Kheirbek et al., 2013; Knierim et al., 2013; McHugh et al., 2007; Wilson et al., 2013).

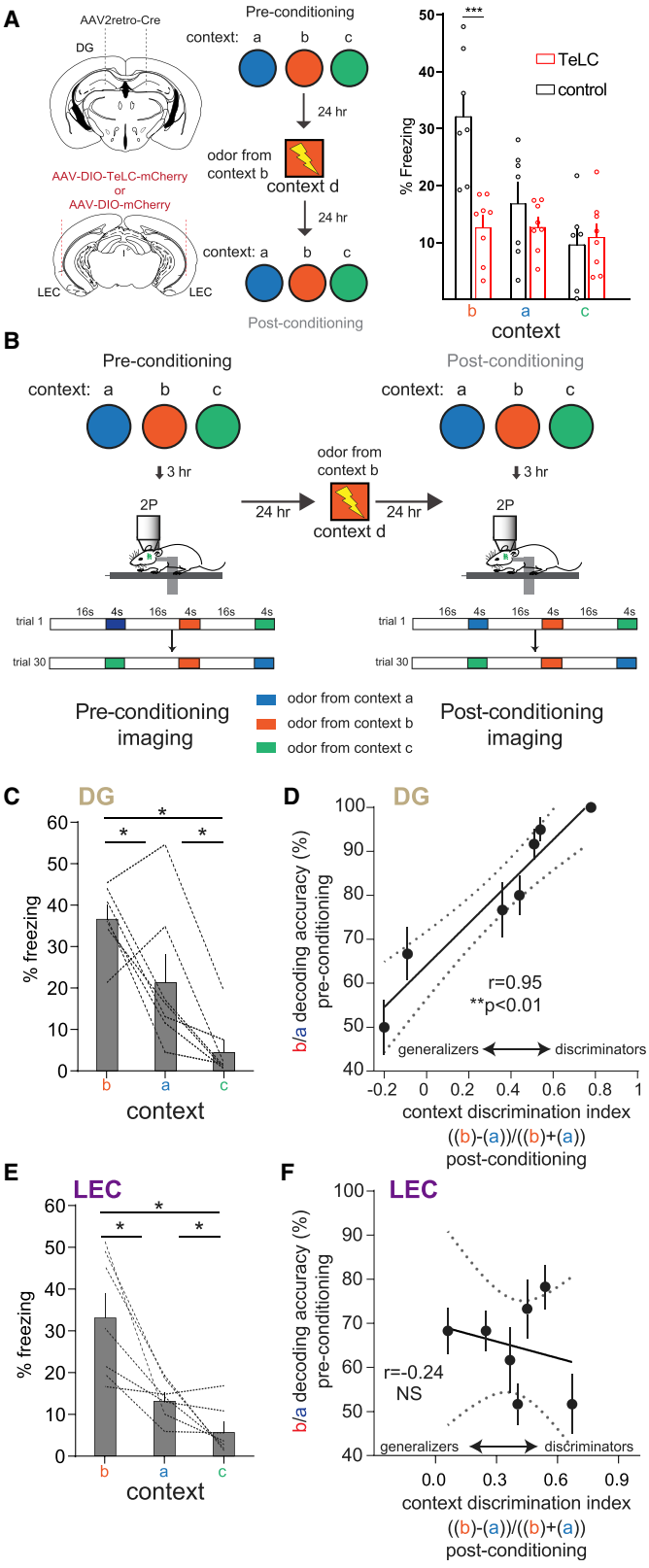

Figure 4. Odor Classification in the DG, but Not LEC, Correlates with Discrimination of Odors for Contextual Recall

(A) LEC-DG TeLC and control mice were pre-exposed to three contexts that differed in the infused odor (context a, ethyl butyrate; b, methyl butyrate; c, isoamyl acetate) to assess pre-conditioning freezing (see Figure S2). The next day, mice were given foot shocks in a novel context infused with the odor from context b (methyl butyrate). 24 h later, mice were re-exposed to contexts a–c and freezing was measured. Right: LEC-DG TeLC showed reduced freezing in the context infused with the odor from the conditioning context (n = 8 LEC-DG TeLC; 7 control; repeated-measures ANOVA with post hoc t test with Holm-Sidak correction; $^{**}p < 0.01$) Error bars represent ± SEM.

(B) Experimental design for imaging. Design was identical as in (A), except that mice were imaged on pre-conditioning and post-conditioning days. Error bars represent ± SEM.

(C) Percent freezing in the DG imaging mice three contexts post-conditioning (n = 7 DG mice; t test with Holm-Sidak correction; $^{*}p < 0.05$). Error bars represent ± SEM.

(D) A context fear discrimination index (context a versus context b) was calculated based on freezing scores for each animal and plotted against the decoding accuracy obtained from 2P imaging pre-conditioning (Pearson's correlation; r = 0.95; n = 7 mice; linear fit with solid line; 95% confidence interval in dashed lines; $p < 0.001$; error bars represent ± SEM for 30 cross validations of the decoder; see STAR Methods).

(E) Percent freezing in the LEC imaging mice in the three contexts post-conditioning (n = 7 LEC mice t test with Holm-Sidak correction; $^{*}p < 0.05$).

(F) Context discrimination indices (context a versus context b) plotted against the decoding accuracies obtained from LEC imaging pre-conditioning. Pearson's correlation; r = −0.24; n = 7 mice; linear fit with solid line; 95% confidence interval in dashed lines; p = 0.3.

Error bars represent ± SEM for 30 cross validations of the decoder (see STAR Methods). For exact p values, see Table S1.

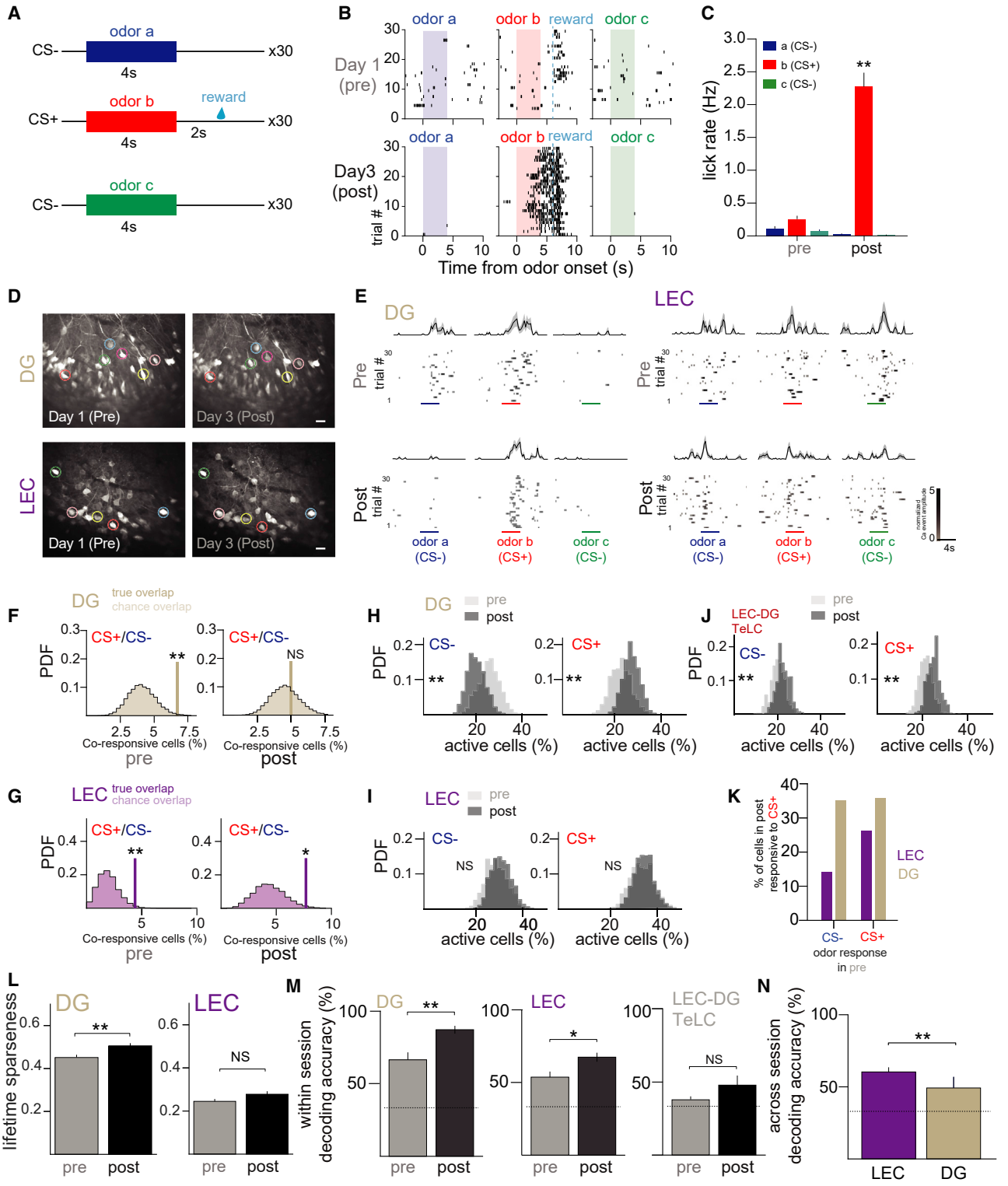

Figure 5. Associative Learning Amplifies Cortical Representations of Salient Stimuli in DG GCs

(A) Experimental schematic for associative odor conditioning. A sucrose reward was delivered on CS+ trials.

(B) Lick rasters showing behavioral performance on day 1 (pre) and day 3 (post) of learning.

(C) Average lick rates during the odor and trace period on day 1 (pre) and day 3 (post; Mann-Whitney U test; **p < 0.01; n = 3 DG mice).

(legend continued on next page)

As the odor present was likely the primary cue that elicited recall of the conditioning context, we asked whether odor decoding accuracy in DG or LEC was related to contextual discrimination post-conditioning. For this, we ran mice in the same protocol, except that we imaged odor responses before (pre) and after (post) conditioning with the footshock. Analysis of context discrimination scores after conditioning revealed considerable individual variability in discrimination of contexts a and b post-conditioning (but not b/c; see Figure S3B), due to the chemical similarity of the EB and MB odorants, as some mice generalized their fear across contexts, although others discriminated (Figures 4C–4E and S3B), similar to that seen in auditory fear discrimination (Likhtik et al., 2014). We thus asked whether behavioral discrimination was correlated with odor classification in the DG and LEC. We computed pairwise context discrimination scores on day 3 (see STAR Methods) to compare to odor decoding accuracy scores. In DG GC recordings, odor decoding accuracy for the similar a/b pair (EB/MB) of odorants before conditioning correlated with context a/b discrimination scores after conditioning, as the mice with lower decoding accuracy scores before conditioning generalized their freezing responses and the mice with the highest neural decoding scores went on to become the best behavioral discriminators (Figure 4D). A similar relationship between neuronal and behavioral discrimination was found when analyzing decoding scores after conditioning or when using similarity of population vectors as a neural readout of discrimination (Figures S3F and S3K). This relationship was only found for the similar a/b (EB/MB) odor pair, in which mice showed individual differences in the level of freezing in the contexts in which these odors were present, as mice were significantly better as a group at behaviorally discriminating the contexts where the distinct odors a/c (EB/IAA) were present. (Figures S3B, S3H, and S3I). This relationship between odor decoding accuracy and contextual discrimination was not seen in mice where recordings were taken from LEC neurons. Although LEC mice showed similar individual variability in the ability to behaviorally discriminate the a/b contexts (Figures 4E and S3B), this did not correlate with neural decoding accuracy scores from LEC before conditioning (Figure 4F). These results show for the first time that the neural discrimination of odor cues in the DG, but not LEC, is correlated with the use of these cues to drive discrimination between contexts.

Changes in Odor Representations in DG and LEC with Reward Learning

Next, we asked how odor representations in DG GCs and LEC change during associative reward learning. We trained mice in an appetitive conditioning task using the same three odors that were used in our context fear discrimination experiment. Odors were delivered for 4 s and then a sucrose reward (unconditioned stimulus [US]) was delivered after a 2-s trace period after presentation of one of the odorants (conditioned stimulus [CS^+], odor b; Figure 5A). We assessed learning by measuring licking during the CS odor/trace period (Figures 5B, 5C, and S4A) and recorded calcium dynamics in DG GCs, LEC neurons, and DG GCs with silenced input from LEC (LEC-DG TeLC mice; as in Figures 3 and 4). Unlike in fear conditioning, where aversive reinforcement is known to drive stimulus generalization (Fletcher and Wilson, 2002; Ghosh and Chattarji, 2015; Likhtik et al., 2014; Pavesi et al., 2012; Resnik and Paz, 2015), mice did not generalize the odor a/b pair, as all mice discriminated by day 3 (Figures 5B, 5C, S5A, and S5B). The same cells in LEC and DG were imaged before learning (pre; day 1) and after odor learning (post; day 3; Figures 5D, 5E, and S4B). First, we found that, before learning, both in DG and LEC, neurons that responded to one odor also tended to respond to another odorant. However, after learning, DG GCs, but not LEC neurons, were less likely to respond to multiple odorants, reducing overlapping odor representations (Figures 5F, 5G, S4C, and S4D). In LEC-DG TeLC mice, in this experiment, we did not find cells that reached the statistical significance cutoff for odor responsivity, again supporting the role of this input in olfactory coding in the DG. In addition to reducing overlap, we found an increase in the proportion of DG GCs that were active during CS^+ odor and a decrease in the number active during the CS− (odor a; Figures 5H and S4E). This again was not observed in LEC neurons (Figure 5I). In LEC-DG TeLC mice, an increase in proportion of active cells was seen indiscriminately during both CS^+ and CS^- odors (Figure 5J). In line with our results in the DG and LEC, by limiting our analysis to those cells that responded to each odor on day 1 (pre), we found that CS^- responsive DG GCs were more likely

(D) Cell registration across days in the same FOV. Circled cells are examples of registered neurons (see STAR Methods and Figure S5 for cell registration approach).
(E) Example rasters and normalized activity for cross registered, odor responsive DG (left) and LEC (right) cells.
(F and G) In the DG (F), odor overlaps for CS^+/CS^- odors fall to levels comparable to the shuffled distribution after learning, but in LEC (G), neurons overlaps remain stable across learning (level of significance for 10,000 shufflings $^{**}p < 0.01$; $^{*}p < 0.05$; n = 359 DG cells; n = 182 LEC cells).
(H–J) Comparison of proportion of active cells during odor presentation in pre and post (pseudo-simultaneous recordings across multiple FOVs, where each bin represents the proportion of odor trials in which we found a given percentage of active cells). Proportion active is significantly increased in the post session for the CS^+ odor and decreased for the CS^- odor in DG (H), but not in LEC (I), and increased to both CS^+ and CS^- odors in (J) LEC-DG TeLC mice (t test; $^{**}p < 0.01$; n = 3 DG mice; n = 3 LEC mice; n = 2 LEC-DG mice).
(K) Odor responses in post for cross-session registered cells. Cells were classified as odor responsive in pre and then their responses were determined in post. Compared to LEC neurons, odor a responsive DG GCs were more likely to become responsive to odor b (CS+ odor) after learning. (n = 3 DG mice, 359 cells; n = 3 LEC mice, 182 cells; X2 test; $p < 0.01$).
(L) Lifetime sparsity increases in DG, but not LEC, across learning (Mann-Whitney; $p < 0.01$; n = 3 DG mice; n = 3 LEC mice).
(M) Odor decoding accuracy improved across learning in both DG and LEC, but not LEC-DG TeLC mice (Mann-Whitney; $^{**}p < 0.01$; $^{*}p < 0.05$; n = 3 DG mice; n = 3 LEC mice; 2 LEC-DG mice).
(N) Across-session odor decoding accuracy (training on pre data and testing on post data) was significantly higher in LEC compared to DG, indicating greater stability in representations within LEC across learning (n = 3 pre group; Mann-Whitney; $^{**}p < 0.01$).
Error bars represent ± SEM. For exact p values, see Table S1.

than LEC neurons to switch their response to the CS^+ odor after learning (Figure 5K). In analysis of populations of DG GCs and LEC neurons, we found that, with learning, odor representations became sparser in the DG, but not LEC (Figure 5L). In addition, odor classification performance prominently increased in the DG, with a more modest increase in LEC (Figure 5M). This again was not seen in LEC-DG TeLC mice, as although these mice could learn this simple association (Figure S4B), odor decoding accuracy in the DG was poor both before and after learning (Figure 5M). Finally, a cross-session decoder performed significantly worse in DG than in LEC (Figure 5N), indicating that the geometry of the population code for odor stimuli in the DG dynamically changes with associative learning. These differential changes in DG and LEC during learning were not due to differences in signal to noise in recordings or differences in lick-related, breathing-related, or reward-related activity between the DG and LEC (Figures S4I–S4L). In addition, increasing the numbers of CS^+ and CS^- odors generated a similar pattern of results in DG GC recordings, as odor decoding accuracy increased with learning (Figure S4H). Finally, we recorded DG GCs during extinction session, where reward was not delivered, and found that odor decoding accuracy was reduced as compared to the post-learning session, raising the intriguing possibility that learning generates new, odor-reward representations in the DG (Figure S4H). Taken together, these results suggest that, during associative learning, LEC provides relatively stable odor representations to DG, where these representations change or generate new odor-reward representations to amplify the contrast between a CS^+ odorant and a CS^- odorant.

DISCUSSION

Here, we have used measures of olfactory coding to show how the DG transforms external sensory stimuli into internal neural representations. We demonstrate that DG GCs effectively encode odor stimulus identities, and this process is correlated with future contextual discrimination. We find that inhibition of input from the LEC impairs odor coding in DG GCs and the use of odor cues to guide contextual recall. By recording in both DG and LEC, we find that odor identity could be more accurately classified from DG GCs than from LEC neurons. In addition, we found that, during olfactory learning, odor representations were more flexible in DG than in LEC. Odor representations dynamically changed in DG, with odor learning inducing an increase in the proportion of cells responding to the CS^+ odorant and a decrease in those responding to the CS^- odorant. This process of expanding the distance in representations with learning may serve as a substrate for memory formation within the DG and downstream HPC regions.

These findings expand upon recent work describing odor representations in upstream areas, such as piriform cortex and olfactory bulb (Bolding and Franks, 2017, 2018; Franks et al., 2011; Iurilli and Datta, 2017; Sosulski et al., 2011; Stettler and Axel, 2009) and studies reporting non-spatial representations in downstream CA1 (Aronov et al., 2017; Hargreaves et al., 2005; Igarashi et al., 2014; McKenzie et al., 2016). Our studies support the hypothesis that every stage of processing along the OB to HPC stream applies some degree of pattern separation to decorrelate odor representations. We find that across odor correlations in DG and LEC are very low, and in some trials, correlations are less than zero, indicating that the LEC-DG circuit strongly separates different odor representations to a greater degree than previously found in OB and piriform cortex (Roland et al., 2017; Schaffer et al., 2018). In addition, we report key differences between odor representations in the DG and those in its primary input region, LEC. Although previous studies in anesthetized mice showed odor-evoked responses in LEC neurons (Leitner et al., 2016), it remained unclear how these responses differ from DG and how they changed with learning. By recording activity in both LEC and DG using a tightly controlled odor-based experimental paradigm, we observed that odor decoding accuracy was better in DG GCs when compared to LEC neurons, which is in line with previous studies proposing a role of DG GCs for an expansion of dimensionality through sparsity (Rolls and Treves, 1998). However, we also found that a model of LEC-DG based on random projections alone was not sufficient to obtain comparable levels of decoding as true DG data. Exploration of other models with random projections that introduce additional non-linearities or ones that incorporate a rich heterogeneity of cell types and plasticity functions (Litwin-Kumar et al., 2017) may more accurately model the expansion of dimensionality and facilitation of associative learning we observe in the DG.

Using an odor-guided contextual fear memory task, we found that, in DG, but not LEC, odor decoding accuracy scores correlated with individual animals' discrimination between contexts that differed in the presented odorant. Mice with the highest odor classification accuracies showed the best discrimination during context recall. In this task, mice use the odor cue for pattern completion: rapid recall of a full contextual representation from the partial cue. Recent studies have highlighted the role of mature DG GCs in pattern-completion-mediated contextual recall (Nakashiba et al., 2012), and our work suggests that LEC-DG input facilitates the use of olfactory information in this process. We found that silencing LEC-DG transmission with TeLC impaired use of the odor cues in a different context to recall the conditioning context, in line with a role for the LEC recognizing non-spatial stimuli that have been experienced in a specific context (Wilson et al., 2013). Although the mechanism for this remains unclear, it may be the case that odor information is separated at the level of the DG and can drive distinct recurrent networks in CA3 to facilitate recall (McNaughton and Morris, 1987; Nakazawa et al., 2002). Thus, in a situation where odors are better separated in the DG, conditioning can drive a distinct CA3 recurrent network state that supports high-fidelity recall and thus effective context discrimination (O'Reilly and McClelland, 1994; Treves and Rolls, 1994). This may explain why odor decoding accuracies in LEC did not correlate with behavioral discrimination, as the added level of separation provided by the DG may be required for fine-tuning CA3 networks. However, future population level imaging studies in CA3 and in LEC-DG projection neurons in odor-guided contextual memory tasks that vary the balance between pattern completion and separation will lend further insight into this process. Silencing LEC-DG transmission, although impairing learning-induced changes in population activity in the DG, did not worsen odor-reward learning in the multi-trial, head-fixed task used here. This would

indicate that either the chronic nature of our silencing leads to compensation by other circuits or that other brain areas or neural circuits are sufficient to perform this kind of associative learning task (Abraham et al., 2012; Boisselier et al., 2014; Gschwend et al., 2015; Han et al., 2018; Igarashi et al., 2014; Komiyama et al., 2010; Lepousez and Lledo, 2013; Li et al., 2017, 2018; Liu et al., 2014; Otazu et al., 2015; Zhu et al., 2018). Use of more temporally precise silencing methods, or more complex behavioral designs, may provide new evidence for the role of LEC-DG in pure odor-reward associations.

We found that CS^+-specific changes that occur in DG during associative learning are less prominent in LEC. The strengthening we observe in neural representations through learning may serve as a substrate for memory formation within the DG and downstream HPC regions. This phenomenon appears as an experience-dependent reduction of dimensionality in DG because the CS^+ odor becomes over represented at the expense of the CS^- odor and odor representations become minimally overlapping, i.e., orthogonal. We did not observe similar changes in LEC, in line with other studies that describe cortical activities as a high-dimensional computational substrate that is useful to flexibly learn new tasks (Fusi et al., 2016; Rigotti et al., 2013). An alternative interpretation may be that, with learning, the DG may generate new odor-reward representations. Studies aimed at manipulating CS-US contingencies and recording LEC and DG population responses will shed light on these different scenarios. Taken together, our experiments have potentially identified a location in a cortex-to-HPC circuit where information is transformed into a format that is potentially behaviorally relevant to the animal. The odor code in the DG becomes more explicit, i.e., by orthogonalizing odor representations, perhaps to allow for easier recall by downstream areas, such as CA3 and CA1, to guide behavior. This may be via plasticity mechanisms at perforant path synapses, neuromodulatory effects on the excitability of DG GCs, or enhancement of local microcircuit function (such as recruitment of adult-generated GCs or local inhibitory/excitatory circuits) to optimize sparsity levels for classification (Drew et al., 2016; Luna et al., 2019). Experiments identifying how any or all of these processes facilitate learning will provide new insight into the ways in which the DG actively classifies odor representation as a consequence of appetitive conditioning. Identification of this process of separating cortical representations of sensory stimuli with learning may represent a novel population-level substrate for associative learning.

Recent work has shown that place cell responses within GCs are stable over days and do not remap in response to global contextual changes (Hainmueller and Bartos, 2018). Thus, although overall spatial maps in the DG remain stable over time, representations of discrete elements of the environment, such as the odorant cues used here, may change with learning, providing downstream areas updated information on the saliency of non-spatial stimuli in the environment. This may reflect differences in the response properties of DG GCs to complex spatial contexts as opposed to specific discrete cues, which may arise from the distinct input pathways to the DG that are activated by spatial versus non-spatial information, with spatially tuned DG GCs relying on medial entorhinal inputs and odor-responsive GCs relying on LEC inputs (Hafting et al., 2005; Hargreaves et al., 2005). In addition, recent work indicates that newly integrated GCs preferentially receive LEC inputs (Vivar et al., 2012; Woods et al., 2018), and this LEC-DG input was recently shown to directly increase the inhibition of mature GCs via adult-born GC activity (Luna et al., 2019), effectively enhancing the sparsity of activation in the DG. Thus, discrete stimuli that recruit LEC over medial entorhinal cortex (MEC) activity may distinctly modulate the activity of downstream mature GCs or selectively drive the highly plastic population of newly integrated GCs (Schmidt-Hieber et al., 2004).

Our findings offer insight to the population level and single-cell encoding properties of the healthy DG, and future studies can leverage these tools to understand how the DG becomes dysfunctional in diseases such as Alzheimer's disease. The earliest aggregation of amyloid-beta plaques in Alzheimer's disease occurs specifically in lateral entorhinal cortex, and hypometabolic-associated cognitive impairment has been localized to the LEC-DG circuit in mouse models and human subjects (Braak and Braak, 1991; Khan et al., 2014). As the loss of sense of smell has been identified as a potent risk factor for development of Alzheimer's disease (Conti et al., 2013; Lafaille-Magnan et al., 2017; Morgan et al., 1995; Vassilaki et al., 2017), it will be of interest to explore how LEC-DG olfactory coding circuits are impacted in early stages of disease progression in mouse models. Taken together, our results suggest that olfactory coding may represent a novel proxy to study memory formation in the hippocampus in health and in disease.

STAR★METHODS

Detailed methods are provided in the online version of this paper and include the following:

- KEY RESOURCES TABLE
- RESOURCE AVAILABILITY
  - Lead Contact
  - Materials Availability
  - Data and Code Availability
- EXPERIMENTAL MODEL AND SUBJECT DETAILS
  - Mice
  - Viral Constructs
- METHOD DETAILS
  - Surgery
  - Post-mortem verification of imaging sites and histological analysis
  - Odor-guided contextual fear memory task
  - Head-fixed odor delivery
  - 2-photon imaging
  - Appetitive Odor Conditioning
  - Calcium data processing
- QUANTIFICATION AND STATISTICAL ANALYSIS
  - Odor responsivity
  - Modulation index
  - Decoding
  - Ensemble similarity
  - Overlaps
  - Lifetime sparseness
  - Signal to noise (SNR)

SUPPLEMENTAL INFORMATION

Supplemental Information can be found online at https://doi.org/10.1016/j.neuron.2020.04.002.

ACKNOWLEDGMENTS

We thank Vikaas Sohal, Zachary Knight, Stefano Fusi, Larry Abbott, Marcus Benna, Ashok Litwin-Kumar, Brett Mensh, and Liam Drew for comments and Thomas McHugh for TeLC plasmid. F.S. was supported by the Kavli Foundation, the NSF's NeuroNex program award DBI-1707398, the Gatsby Charitable Foundation, and the Swartz Foundation. J.S.B. was supported by the Brain and Behavioral Research Foundation (NARSAD). M.A.K. was supported by NIMH (R01 MH108623, R01 MH111754, and R01 MH117961), a Weill Scholar Award, a One Mind Rising Star Award, the Human Frontier Science Program, the Esther A. and Joseph Klingenstein Fund, and the Pew Charitable Trusts.

AUTHOR CONTRIBUTIONS

Conceptualization and Writing, N.I.W., F.S., and M.A.K.; Methodology, N.I.W., J.S.B., and M.A.K.; Investigation, N.I.W., D.L.A.-M., and I.M.C.T.; Formal Analysis, N.I.W., F.S., and M.A.K.; Supervision and Funding Acquisition, M.A.K.

DECLARATION OF INTERESTS

The authors declare no competing interests.

Received: August 15, 2019
Revised: March 16, 2020
Accepted: March 31, 2020
Published: April 30, 2020

REFERENCES

Abraham, N.M., Guerin, D., Bhaukaurally, K., and Carleton, A. (2012). Similar odor discrimination behavior in head-restrained and freely moving mice. PLoS ONE *7*, e51789.

Abusaad, I., MacKay, D., Zhao, J., Stanford, P., Collier, D.A., and Everall, I.P. (1999). Stereological estimation of the total number of neurons in the murine hippocampus using the optical disector. J. Comp. Neurol. *408*, 560–566.

Aimone, J.B., Deng, W., and Gage, F.H. (2011). Resolving new memories: a critical look at the dentate gyrus, adult neurogenesis, and pattern separation. Neuron *70*, 589–596.

Aronov, D., Nevers, R., and Tank, D.W. (2017). Mapping of a non-spatial dimension by the hippocampal-entorhinal circuit. Nature *543*, 719–722.

Barak, O., Rigotti, M., and Fusi, S. (2013). The sparseness of mixed selectivity neurons controls the generalization–discrimination trade-off. Journal of Neuroscience *33*, 3844–3856.

Basu, J., Zaremba, J.D., Cheung, S.K., Hitti, F.L., Zemelman, B.V., Losonczy, A., and Siegelbaum, S.A. (2016). Gating of hippocampal activity, plasticity, and memory by entorhinal cortex long-range inhibition. Science *351*, aaa5694.

Bathellier, B., Buhl, D.L., Accolla, R., and Carleton, A. (2008). Dynamic ensemble odor coding in the mammalian olfactory bulb: sensory information at different timescales. Neuron *57*, 586–598.

Bishop, C. (2006). Pattern Recognition and Machine Learning (Springer-Verlag New York).

Boehringer, R., Polygalov, D., Huang, A.J.Y., Middleton, S.J., Robert, V., Wintzer, M.E., Piskorowski, R.A., Chevaleyre, V., and McHugh, T.J. (2017). Chronic loss of CA2 transmission leads to hippocampal hyperexcitability. Neuron *94*, 642–655.e9.

Boisselier, L., Ferry, B., and Gervais, R. (2014). Involvement of the lateral entorhinal cortex for the formation of cross-modal olfactory-tactile associations in the rat. Hippocampus *24*, 877–891.

Bolding, K.A., and Franks, K.M. (2017). Complementary codes for odor identity and intensity in olfactory cortex. eLife *6*, e22630.

Bolding, K.A., and Franks, K.M. (2018). Recurrent cortical circuits implement concentration-invariant odor coding. Science *361*, eaat6904.

Braak, H., and Braak, E. (1991). Neuropathological stageing of Alzheimer-related changes. Acta Neuropathol. *82*, 239–259.

Broca, P. (1878). Anatomie Compared des Circonvolutions Cerebrales (Le Grand Lobe).

Conti, M.Z., Vicini-Chilovi, B., Riva, M., Zanetti, M., Liberini, P., Padovani, A., and Rozzini, L. (2013). Odor identification deficit predicts clinical conversion from mild cognitive impairment to dementia due to Alzheimer's disease. Arch. Clin. Neuropsychol. *28*, 391–399.

Danielson, N.B., Kaifosh, P., Zaremba, J.D., Lovett-Barron, M., Tsai, J., Denny, C.A., Balough, E.M., Goldberg, A.R., Drew, L.J., Hen, R., et al. (2016). Distinct contribution of adult-born hippocampal granule cells to context encoding. Neuron *90*, 101–112.

Drew, L.J., Kheirbek, M.A., Luna, V.M., Denny, C.A., Cloidt, M.A., Wu, M.V., Jain, S., Scharfman, H.E., and Hen, R. (2016). Activation of local inhibitory circuits in the dentate gyrus by adult-born neurons. Hippocampus *26*, 763–778.

Eichenbaum, H., and Otto, T. (1992). The hippocampus and the sense of smell. In Chemical Signals in Vertebrates 6, R.L. Doty, D. Müller-Schwarze, and M.A. Boston, eds. (Springer), pp. 67–77.

Eichenbaum, H., Yonelinas, A.P., and Ranganath, C. (2007). The medial temporal lobe and recognition memory. Annu. Rev. Neurosci. *30*, 123–152.

Fletcher, M.L., and Wilson, D.A. (2002). Experience modifies olfactory acuity: acetylcholine-dependent learning decreases behavioral generalization between similar odorants. J. Neurosci. *22*, RC201.

Franks, K.M., Russo, M.J., Sosulski, D.L., Mulligan, A.A., Siegelbaum, S.A., and Axel, R. (2011). Recurrent circuitry dynamically shapes the activation of piriform cortex. Neuron *72*, 49–56.

Fusi, S., Miller, E.K., and Rigotti, M. (2016). Why neurons mix: high dimensionality for higher cognition. Curr. Opin. Neurobiol. *37*, 66–74.

Ghosh, S., and Chattarji, S. (2015). Neuronal encoding of the switch from specific to generalized fear. Nat. Neurosci. *18*, 112–120.

Gschwend, O., Abraham, N.M., Lagier, S., Begnaud, F., Rodriguez, I., and Carleton, A. (2015). Neuronal pattern separation in the olfactory bulb improves odor discrimination learning. Nat. Neurosci. *18*, 1474–1482.

Hafting, T., Fyhn, M., Molden, S., Moser, M.-B., and Moser, E.I. (2005). Microstructure of a spatial map in the entorhinal cortex. Nature *436*, 801–806.

Hainmueller, T., and Bartos, M. (2018). Parallel emergence of stable and dynamic memory engrams in the hippocampus. Nature *558*, 292–296.

Han, Z., Zhang, X., Zhu, J., Chen, Y., and Li, C.T. (2018). High-throughput automatic training system for odor-based learned behaviors in head-fixed mice. Front. Neural Circuits *12*, 15.

Hargreaves, E.L., Rao, G., Lee, I., and Knierim, J.J. (2005). Major dissociation between medial and lateral entorhinal input to dorsal hippocampus. Science *308*, 1792–1794.

Heale, V.R., and Vanderwolf, C.H. (1994). Dentate gyrus and olfactory bulb responses to olfactory and noxious stimulation in urethane anaesthetized rats. Brain Res. *652*, 235–242.

Heale, V.R., and Vanderwolf, C.H. (1999). Odor-induced fast waves in the dentate gyrus depend on a pathway through posterior cerebral cortex: effects of limbic lesions and trimethyltin. Brain Res. Bull. *50*, 291–299.

Igarashi, K.M., Lu, L., Colgin, L.L., Moser, M.-B., and Moser, E.I. (2014). Coordination of entorhinal-hippocampal ensemble activity during associative learning. Nature *510*, 143–147.

Iurilli, G., and Datta, S.R. (2017). Population coding in an innately relevant olfactory area. Neuron *93*, 1180–1197.e7.

Khan, U.A., Liu, L., Provenzano, F.A., Berman, D.E., Profaci, C.P., Sloan, R., Mayeux, R., Duff, K.E., and Small, S.A. (2014). Molecular drivers and cortical spread of lateral entorhinal cortex dysfunction in preclinical Alzheimer's disease. Nat. Neurosci. *17*, 304–311.

Kheirbek, M.A., Drew, L.J., Burghardt, N.S., Costantini, D.O., Tannenholz, L., Ahmari, S.E., Zeng, H., Fenton, A.A., and Hen, R. (2013). Differential control of learning and anxiety along the dorsoventral axis of the dentate gyrus. Neuron *77*, 955–968.

Knierim, J.J., and Neunuebel, J.P. (2016). Tracking the flow of hippocampal computation: pattern separation, pattern completion, and attractor dynamics. Neurobiol. Learn. Mem. *129*, 38–49.

Knierim, J.J., Neunuebel, J.P., and Deshmukh, S.S. (2013). Functional correlates of the lateral and medial entorhinal cortex: objects, path integration and local-global reference frames. Philos. Trans. R. Soc. Lond. B Biol. Sci. *369*, 20130369.

Komiyama, T., Sato, T.R., O'Connor, D.H., Zhang, Y.-X., Huber, D., Hooks, B.M., Gabitto, M., and Svoboda, K. (2010). Learning-related fine-scale specificity imaged in motor cortex circuits of behaving mice. Nature *464*, 1182–1186.

Krettek, J.E., and Price, J.L. (1977). Projections from the amygdaloid complex and adjacent olfactory structures to the entorhinal cortex and to the subiculum in the rat and cat. J. Comp. Neurol. *172*, 723–752.

Lafaille-Magnan, M.-E., Poirier, J., Etienne, P., Tremblay-Mercier, J., Frenette, J., Rosa-Neto, P., and Breitner, J.C.S.; PREVENT-AD Research Group (2017). Odor identification as a biomarker of preclinical AD in older adults at risk. Neurology *89*, 327–335.

Leitner, F.C., Melzer, S., Lütcke, H., Pinna, R., Seeburg, P.H., Helmchen, F., and Monyer, H. (2016). Spatially segregated feedforward and feedback neurons support differential odor processing in the lateral entorhinal cortex. Nat. Neurosci. *19*, 935–944.

Lepousez, G., and Lledo, P.-M. (2013). Odor discrimination requires proper olfactory fast oscillations in awake mice. Neuron *80*, 1010–1024.

Li, Y., Xu, J., Liu, Y., Zhu, J., Liu, N., Zeng, W., Huang, N., Rasch, M.J., Jiang, H., Gu, X., et al. (2017). A distinct entorhinal cortex to hippocampal CA1 direct circuit for olfactory associative learning. Nat. Neurosci. *20*, 559–570.

Li, W.L., Chu, M.W., Wu, A., Suzuki, Y., Imayoshi, I., and Komiyama, T. (2018). Adult-born neurons facilitate olfactory bulb pattern separation during task engagement. eLife *7*, e33006.

Likhtik, E., Stujenske, J.M., Topiwala, M.A., Harris, A.Z., and Gordon, J.A. (2014). Prefrontal entrainment of amygdala activity signals safety in learned fear and innate anxiety. Nat. Neurosci. *17*, 106–113.

Litwin-Kumar, A., Harris, K.D., Axel, R., Sompolinsky, H., and Abbott, L.F. (2017). Optimal degrees of synaptic connectivity. Neuron *93*, 1153–1164.e7.

Liu, D., Gu, X., Zhu, J., Zhang, X., Han, Z., Yan, W., Cheng, Q., Hao, J., Fan, H., Hou, R., et al. (2014). Medial prefrontal activity during delay period contributes to learning of a working memory task. Science *346*, 458–463.

Luna, V.M., Anacker, C., Burghardt, N.S., Khandaker, H., Andreu, V., Millette, A., Leary, P., Ravenelle, R., Jimenez, J.C., Mastrodonato, A., et al. (2019). Adult-born hippocampal neurons bidirectionally modulate entorhinal inputs into the dentate gyrus. Science *364*, 578–583.

MacDonald, C.J., Carrow, S., Place, R., and Eichenbaum, H. (2013). Distinct hippocampal time cell sequences represent odor memories in immobilized rats. J. Neurosci. *33*, 14607–14616.

Martin, C., Beshel, J., and Kay, L.M. (2007). An olfacto-hippocampal network is dynamically involved in odor-discrimination learning. J. Neurophysiol. *98*, 2196–2205.

McHugh, T.J., Jones, M.W., Quinn, J.J., Balthasar, N., Coppari, R., Elmquist, J.K., Lowell, B.B., Fanselow, M.S., Wilson, M.A., and Tonegawa, S. (2007). Dentate gyrus NMDA receptors mediate rapid pattern separation in the hippocampal network. Science *317*, 94–99.

McKenzie, S., Keene, C.S., Farovik, A., Bladon, J., Place, R., Komorowski, R., and Eichenbaum, H. (2016). Representation of memories in the cortical-hippocampal system: results from the application of population similarity analyses. Neurobiol. Learn. Mem. *134* (Pt A), 178–191.

McNaughton, B.L., and Morris, R.G.M. (1987). Hippocampal synaptic enhancement and information storage within a distributed memory system. Trends Neurosci. *10*, 408–415.

McNaughton, B.L., Battaglia, F.P., Jensen, O., Moser, E.I., and Moser, M.-B. (2006). Path integration and the neural basis of the 'cognitive map'. Nat. Rev. Neurosci. *7*, 663–678.

Meister, M., and Bonhoeffer, T. (2001). Tuning and topography in an odor map on the rat olfactory bulb. J. Neurosci. *21*, 1351–1360.

Morgan, C.D., Nordin, S., and Murphy, C. (1995). Odor identification as an early marker for Alzheimer's disease: impact of lexical functioning and detection sensitivity. J. Clin. Exp. Neuropsychol. *17*, 793–803.

Nakashiba, T., Cushman, J.D., Pelkey, K.A., Renaudineau, S., Buhl, D.L., McHugh, T.J., Rodriguez Barrera, V., Chittajallu, R., Iwamoto, K.S., McBain, C.J., et al. (2012). Young dentate granule cells mediate pattern separation, whereas old granule cells facilitate pattern completion. Cell *149*, 188–201.

Nakazawa, K., Quirk, M.C., Chitwood, R.A., Watanabe, M., Yeckel, M.F., Sun, L.D., Kato, A., Carr, C.A., Johnston, D., Wilson, M.A., and Tonegawa, S. (2002). Requirement for hippocampal CA3 NMDA receptors in associative memory recall. Science *297*, 211–218.

O'Reilly, R.C., and McClelland, J.L. (1994). Hippocampal conjunctive encoding, storage, and recall: avoiding a trade-off. Hippocampus *4*, 661–682.

Olton, D.S., Becker, J.T., and Handelmann, G.E. (1979). Hippocampus, space, and memory. Behav. Brain Sci. *2*, 313–322.

Otazu, G.H., Chae, H., Davis, M.B., and Albeanu, D.F. (2015). Cortical feedback decorrelates olfactory bulb output in awake mice. Neuron *86*, 1461–1477.

Pavesi, E., Gooch, A., Lee, E., and Fletcher, M.L. (2012). Cholinergic modulation during acquisition of olfactory fear conditioning alters learning and stimulus generalization in mice. Learn. Mem. *20*, 6–10.

Pedregosa, F., Varoquaux, G., Gramfort, A., Michel, V., Thirion, B., Grisel, O., Blondel, B., Prettenhofer, P., Weiss, R., Dubourg, V., Vanderplas, J., Passos, A., Cournapeau, D., Brucher, M., Perrot, M., and Duchesnay, E. (2011). Scikit-learn: Machine Learning in Python. Journal of Machine Learning Research *12*, 2825–2830.

Resnik, J., and Paz, R. (2015). Fear generalization in the primate amygdala. Nat. Neurosci. *18*, 188–190.

Rigotti, M., Barak, O., Warden, M.R., Wang, X.-J., Daw, N.D., Miller, E.K., and Fusi, S. (2013). The importance of mixed selectivity in complex cognitive tasks. Nature *497*, 585–590.

Roland, B., Deneux, T., Franks, K.M., Bathellier, B., and Fleischmann, A. (2017). Odor identity coding by distributed ensembles of neurons in the mouse olfactory cortex. eLife *6*, e26337.

Rolls, E.T., and Tovee, M.J. (1995). Sparseness of the neuronal representation of stimuli in the primate temporal visual cortex. J. Neurophysiol. *73*, 713–726.

Rolls, E.T., and Treves, A. (1998). Neural Networks and Brain Function (Oxford University).

Room, P., Groenewegen, H.J., and Lohman, A.H.M. (1984). Inputs from the olfactory bulb and olfactory cortex to the entorhinal cortex in the cat. I. Anatomical observations. Exp. Brain Res. *56*, 488–496.

Sahay, A., Wilson, D.A., and Hen, R. (2011). Pattern separation: a common function for new neurons in hippocampus and olfactory bulb. Neuron *70*, 582–588.

Schaffer, E.S., Stettler, D.D., Kato, D., Choi, G.B., Axel, R., and Abbott, L.F. (2018). Odor perception on the two sides of the brain: consistency despite randomness. Neuron *98*, 736–742.e3.

Schmidt-Hieber, C., Jonas, P., and Bischofberger, J. (2004). Enhanced synaptic plasticity in newly generated granule cells of the adult hippocampus. Nature *429*, 184–187.

Sheintuch, L., Rubin, A., Brande-Eilat, N., Geva, N., Sadeh, N., Pinchasof, O., and Ziv, Y. (2017). Tracking the same neurons across multiple days in Ca^{2+} imaging data. Cell Rep. *21*, 1102–1115.

Shipley, M.T., and Adamek, G.D. (1984). The connections of the mouse olfactory bulb: a study using orthograde and retrograde transport of wheat germ agglutinin conjugated to horseradish peroxidase. Brain Res. Bull. *12*, 669–688.

Sosulski, D.L., Bloom, M.L., Cutforth, T., Axel, R., and Datta, S.R. (2011). Distinct representations of olfactory information in different cortical centres. Nature *472*, 213–216.

Stettler, D.D., and Axel, R. (2009). Representations of odor in the piriform cortex. Neuron *63*, 854–864.

Treves, A., and Rolls, E.T. (1994). Computational analysis of the role of the hippocampus in memory. Hippocampus *4*, 374–391.

Tulving, E., and Markowitsch, H.J. (1998). Episodic and declarative memory: role of the hippocampus. Hippocampus *8*, 198–204.

Uchida, N., and Mainen, Z.F. (2003). Speed and accuracy of olfactory discrimination in the rat. Nat. Neurosci. *6*, 1224–1229.

Vanderwolf, C.H. (1992). Hippocampal activity, olfaction, and sniffing: an olfactory input to the dentate gyrus. Brain Res. *593*, 197–208.

Vassilaki, M., Christianson, T.J., Mielke, M.M., Geda, Y.E., Kremers, W.K., Machulda, M.M., Knopman, D.S., Petersen, R.C., Lowe, V.J., Jack, C.R., Jr., and Roberts, R.O. (2017). Neuroimaging biomarkers and impaired olfaction in cognitively normal individuals. Ann. Neurol. *81*, 871–882.

Vinje, W.E., and Gallant, J.L. (2000). Sparse coding and decorrelation in primary visual cortex during natural vision. Science *287*, 1273–1276.

Vivar, C., Potter, M.C., Choi, J., Lee, J.-Y., Stringer, T.P., Callaway, E.M., Gage, F.H., Suh, H., and van Praag, H. (2012). Monosynaptic inputs to new neurons in the dentate gyrus. Nat. Commun. *3*, 1107.

Wilson, R.C., and Steward, O. (1978). Polysynaptic activation of the dentate gyrus of the hippocampal formation: an olfactory input via the lateral entorhinal cortex. Exp. Brain Res. *33*, 523–534.

Wilson, D.I.G., Watanabe, S., Milner, H., and Ainge, J.A. (2013). Lateral entorhinal cortex is necessary for associative but not nonassociative recognition memory. Hippocampus *23*, 1280–1290.

Witter, M.P., Doan, T.P., Jacobsen, B., Nilssen, E.S., and Ohara, S. (2017). Architecture of the entorhinal cortex a review of entorhinal anatomy in rodents with some comparative notes. Front. Syst. Neurosci. *11*, 46.

Woods, N.I., Vaaga, C.E., Chatzi, C., Adelson, J.D., Collie, M.F., Perederiy, J.V., Tovar, K.R., and Westbrook, G.L. (2018). Preferential targeting of lateral entorhinal inputs onto newly integrated granule cells. J. Neurosci. *38*, 5843–5853.

Xu, W., and Wilson, D.A. (2012). Odor-evoked activity in the mouse lateral entorhinal cortex. Neuroscience *223*, 12–20.

Yassa, M.A., and Stark, C.E.L. (2011). Pattern separation in the hippocampus. Trends Neurosci. *34*, 515–525.

Zhou, P., Resendez, S.L., Rodriguez-Romaguera, J., Jimenez, J.C., Neufeld, S.Q., Giovannucci, A., Friedrich, J., Pnevmatikakis, E.A., Stuber, G.D., Hen, R., et al. (2018). Efficient and accurate extraction of in vivo calcium signals from microendoscopic video data. eLife *7*, e28728.

Zhu, Y., Nachtrab, G., Keyes, P.C., Allen, W.E., Luo, L., and Chen, X. (2018). Dynamic salience processing in paraventricular thalamus gates associative learning. Science *362*, 423–429.

STAR★METHODS

KEY RESOURCES TABLE

REAGENT or RESOURCE	SOURCE	IDENTIFIER
Bacterial and Virus Strains		
AAVdj-EF1a-DIO-TeLC-mCherry	Boehringer et al., 2017	N/A
AAVdj-EF1a-DIO-mCherry	Boehringer et al., 2017	N/A
AAVdj-CamKIIa-GCaMP 6f	Stanford Vector Core	Cat# GVVC-AAV-90
AAV2retro-CAG-Cre	UNC Vector Core	https://www.med.unc.edu/genetherapy/jvl.htm
Experimental Models: Organisms/Strains		
C57BL/6J mice	Jackson Laboratory	Cat#000664; RRID:SCR_004633; http://www.jax.org/
Software and Algorithms		
MATLAB	Mathworks	https://www.mathworks.com/products/matlab.html; RRID:SCR_001622
CNMF-E	Zhou et al., 2018	https://github.com/zhoupc/CNMF_E
FreezeFrame	Coulbourn Instruments	Cat#ACT-100A; RRID:SCR_014429; https://www.actimetrics.com/products/freezeframe/
Prism 8	GraphPad	https://www.graphpad.com/scientific-software/prism/
Illustrator	Adobe	https://www.adobe.com/products/illustrator.html; RRID:SCR_010279
Scikit-learn (Python)	Pedregosa et al., 2011	https://scikit-learn.org

RESOURCE AVAILABILITY

Lead Contact

Further information and requests for resources and reagents should be directed to and will be fulfilled by the Lead Contact, Mazen Kheirbek (Mazen.Kheirbek@ucsf.edu).

Materials Availability

This study did not generate new unique reagents.

Data and Code Availability

The datasets and analysis code supporting the current study are available from the lead contact on request.

EXPERIMENTAL MODEL AND SUBJECT DETAILS

Mice

All procedures were conducted in accordance with the U.S. NIH Guide for the Care and Use of Laboratory Animals and the institutional Animal Care and Use Committees at UCSF. Adult male C57BL/6J mice were supplied by Jackson Laboratory and were used beginning at 8-12 weeks of age. Mice were co-housed with litter mates (2-5 per cage). Mice were maintained with unrestricted access to food and water on a 12-hour light/dark cycle and experiments were conducted during the dark cycle portion.

Viral Constructs

For calcium imaging, AAVdj-CaMKII-GCaMP6f-WPRE-SV40 was packaged and supplied by Stanford Viral Vector Core at titer of 2.05 X 10^13 vg/ml. For tetanus toxin experiments, AAV-EF1a-DIO-TeLC-mCherry and AAV-EF1a-DIO-mCherry plasmids (Boehringer et al., 2017) were generously provided by Dr. Thomas McHugh (RIKEN) and packaged into AAVdj at Stanford Vector Core at a titer of 1.92 X 10^12 vg/ml and 6.34 × 10^12 vg/ml, respectively. AAV2retro-CAG-Cre was packaged and supplied by UNC Vector Core and injected at a titer of 2.8 × 10^12 vg/ml.

METHOD DETAILS

Surgery

Animals were 8-12 weeks of age at time of initial viral injection surgery. Mice were anesthetized with 1.5% isoflurane with an oxygen flow rate of ~1 L / min, and head-fixed in a stereotactic frame (David Kopf, Tujunga, CA). Eyes were lubricated with an ophthalmic ointment, and body temperature was maintained at 34-37°C with a warm water re-circulator (Stryker, Kalamazoo, MI). Fur was shaved and incision site sterilized with isopropyl alcohol three times and betadine solution three times prior to beginning surgical procedures. Lidocaine HCl 2% solution was injected subcutaneously local to incision, and post-surgical analgesia was provided by meloxicam and slow-release buprenorphine. For calcium imaging experiments, viral injections preceded lens implantation by 2-3 weeks to allow viral expression. For stereotactic viral injections, a craniotomy was made at injection site with a round 0.5 mm drill bit (David Kopf, Tujunga, CA). A nanoject syringe (Drummond Scientific, Broomall, PA) was used with a pulled glass pipette (tip width 20-30 microns) to inject a total of 483 nL of AAVdj-CaMKII-GCaMP6f-WPRE-SV40 into the dorsal dentate gyrus at coordinates of AP −2.15, ML ± 1.25, DV −2.3, −2.15, −2.05, all relative to bregma (Paxinos and Franklin's, 4th edition). At each dorsal-ventral site of the dentate gyrus, 5 × 32.2nl pulses were delivered separated by 10 s. The needle was held in place for 5 minutes prior to moving to the next D/V coordinate, and remained in place for 10 minutes following the final injection before being slowly withdrawn from the brain. For injections into lateral entorhinal cortex, the following coordinates were used: AP −3.6, ML ± 4.4 (AP and ML coordinates from bregma), DV −2.6 (from medial brain surface at craniotomy site). For LEC-DG TeLC experiments, AAV2retro-CAG-Cre and AAV-EF1a-DIO-TeLC-mCherry/AAV-EF1a-DIO-mCherry were injected bilaterally into the DG and LEC respectively at the same volume as GCaMP injections.

We modified a previously published procedure for imaging DG GCs, which has been shown to preserve DG structure, activity and DG-dependent behaviors (Danielson et al., 2016). Lens implantation surgery occurred 2-3 weeks following GCaMP6f virus injection. 30 minutes prior to anesthesia, dexamethasone was injected subcutaneously (0.2mg/kg dissolved in sterile saline). The animal was prepared on the stereotax as mentioned above. After making a longitudinal midline incision exposing the upper extent of the cranium, a no. 15 scalpel blade was used to scrape periosteum from the skull surface, as well as most superficial (~0.5mm) of posterior neck muscles attaching to the dorsal portion of the caudal skull surface. The skull surface was wiped with hydrogen peroxide for 15 s to further remove residual periosteum, then rinsed 3x with saline. Finally, the skull was lightly scored with a scalpel blade in a cross-hatched pattern to increase surface area contact for dental acrylic. A craniotomy approximating 1.1 mm in diameter was drilled by hand with a rounded drill bit centered on the same AP (−2.15) and ML (−1.25) coordinates as the GCaMP injection for DG. For LEC, the craniotomy was made at AP (−3.6) and ML (−4.4). Dura was removed with a fish-hooked 27 gauge needle, and a 30 gauge blunt end needle was used to aspirate neural tissue superficial of the dentate gyrus or lateral entorhinal cortex. For DG surgeries, the hippocampal fissure surface was used to determine proper aspiration depth. For LEC implantation, 1mm of cortex was aspirated above implant location, estimated by marked depth on aspiration needle. The cranial cavity was filled with saline and collagen hemostat (Avitene) for 10 mins or until bleeding ceased when collagen plug was removed. The cavity was re-filled with saline, and a 1mm wide x 4.1mm long ProView GRIN lens (GLP-1042, Inscopix, Palo Alto, CA) was stereotactically implanted (AP −2.15, ML −1.25, DV −1.95) above the dentate gyrus,or LEC (AP −3.6, ML −4.4, DV −2 from skull surface at craniotomy). A miniaturized microscope (Inscopix) was used for visual guidance and fluorescence monitoring, and once placed, the lens was fixed to the skull with Metabond adhesive cement (Parkell, Edgewood, NY). The lens was lowered with an electronically controlled stereotax arm attachment (Scientifica, Uckfield, UK), and lowered at a rate of 0.2 mm per min until target depth was reached. Final depth was adjusted within 0.1 mm of target depth based upon maximizing the quality of the visualized fluorescence signal. Animals without fluorescence visible thru the miniscope were not used and lenses were retrieved. A custom-made titanium headbar was then attached to the skull using dental cement (Dentsply Sinora, Philadelphia, PA). Finally, a protective cap over the lens was applied with Kwik-Sil silicone elastomer (World Precision Instruments, Sarasota, Fl), which was removed and re-applied for each imaging session. Mice were allowed to recover from lens implant surgery for at least 2 weeks prior to imaging experiments.

Post-mortem verification of imaging sites and histological analysis

DG and LEC imaging sites were verified in each animal included in final analysis (Figure S1). After imaging, mice were perfused transcardially with PBS followed by 4% PFA (both ~20 mL at a rate of 7-8ml per min). Entire mouse heads were placed in 4% PFA solution for 2-3 days to allow ample fixation of the area around the lens, allowing for dissection with the lens indent intact. Serial coronal sections (50 microns) around the lens site were collected and visualized and cross-registered with a mouse brain atlas.

For LEC-DG TeLC silencing experiments, animals were perfused as noted above, and a 1-in-6 series of coronal sections (50 microns) were collected. TeLC-mCherry expressing cell counts in the lateral entorhinal cortex were assessed for each mouse by identifying the section nearest to the targeted stereotactic injection (AP −3.6) site based on cross-registering with the Allen Brain Atlas, then counting the mCherry positive cells within the lateral entorhinal cortex to establish a total cell count for each animal, normalized by tissue area. An average count per mouse is provided and each mouse was verified for mCherry expression delimited to LEC cells projecting to DG (and not CA1) by visualizing mCherry positive terminals within the outer molecular layer of the dentate gyrus (Figure S1).

Odor-guided contextual fear memory task

Mice were run through a three day odor-guided contextual fear memory paradigm, where on day 1 mice were exposed to 3 contexts (Pre-conditioning), day 2 were conditioned in a different context (Conditioning), and day 3 tested in the same 3 contexts as day 1 (Post-conditioning). In imaging experiments, on Pre-conditioning and Post-conditioning days, mice were exposed to the contexts in the AM, then imaged with 2-photon microscopy in the PM (three hours after last context exposure). On day 1 and 3 (Pre-conditioning and Post-conditioning), mice were placed in a standard fear conditioning box (MedAssociates, Fairfax VT) with the following contextual cues: acrylic floor and rounded walls, floor with alpha-dry bedding, lights off, fan off, and ambient white noise at 60 dB. Each pre-conditioning and post-conditioning context differed in the presence of the odors, one of 3 odors was present below the grid floor (odor a: ethyl butyrate, odor b: methyl butyrate, odor c: isoamyl acetate). Odors were applied directly to a clean cotton tip applicator for a few seconds until saturated, and placed under grating 1-2 minutes prior to an animals' entry into the conditioning box. One hour separated each context exposure, and odorant was cleared from room with a charcoal vacuum filter, and order of exposure was randomized among mice. For pre and post conditioning, mice were allowed to explore the context for 5 mins before removal, and percent freezing was evaluated. On conditioning day, the mice were placed in the fear conditioning boxes with odor b (methyl butyrate) present, and the following contextual cues: (conditioning context (context d): bare metal grating floor, squared walls, lights on, fan on, room lights on). Mice were allowed to explore the context for 3 minutes prior to receiving three footshocks 60 s apart (2 s, 0.7mA). After the final shock, mice were immediately removed from the shock box. Behavioral freezing data was collected and analyzed using FreezeFrame video software (Actimetrics) with a freezing epoch threshold of 1 s, and automatic movement signal detection. Freezing percentages represent the entire 5 minutes of re-exposure and were performed with the experimenter blind to odor or experimental group. Context discrimination index for any context pair was calculated as (percent time freezing to context 1- percent time freezing to context 2)/(percent time freezing to context 1+ percent time freezing to context 2).

Head-fixed odor delivery

Animals were handled and habituated to the experimenter, training environment and head-fixation setup for 30 mins a day for at least two days before imaging experiments were ran. On imaging days, monomolecular odors were delivered through a custom built 6 channel olfactometer equipped with a mass flow controller (Alicat Scientific, Tucson, AZ) that monitored and maintained air flow at 2 l per min and prevented momentary pressure changes from solenoid valve switches upstream of the controller. The olfactometer solenoids were triggered by an Arduino Mega with custom circuit boards (http://OpenMaze.org), and stimulus delivery recorded via CoolTerm software. One side of the nose cone had a tubing insert that delivered odors, the other side containing an outlet in which a gentle vacuum was applied to evacuate residual odor. Additionally, an ongoing charcoal filter vacuum system (Hydrobuilders Inc.) was placed in the 2P isolation box to evacuate odors that leaked out of the nosecone apparatus. For all experiments, mice were habituated to the 2p head fixed setup for 10 mins prior to imaging, and imaged for 30 s at baseline before a structured trial of odors were delivered for 4 s with a 16 s ITI, presented in pseudo-randomized fashion. For 6 odor experiments, 20 trials were performed for each odor for a total continuous imaging session of ~30 mins. For 3 odor experiments, 30 presentations of each odor were performed in a session (~30 mins). Several different odor panels were run on cohorts of imaged animals. For a 6 neutral odor panel (Figures 1, 2, and 3), we used: benzaldehyde (BA), eugenol (EU), heptanal (HEP), hexanal (HEX), alpha-pinene (PIN), and eucalyptol (EUC). For a 3 odor panel testing odor discrimination and learning (Figures 4 and 5) we used methyl butyrate (MB) ethyl butyrate (EB) and isoamyl acetate (IAA). For mixed tone/odor experiments (Figure S1), mice were given 3 tones at 4, 9 and 10Khz, 4 s each with 16 s ITI presented in a pseudorandom order, 30 presentations each, identical in trial design to the 3 odor experiment. Following tone trials (in the same session), the same FOV was recorded for 3 odor responses as above (EB, MB, IAA) so that we could directly compare overlapping tone/odor responses within the same population of neurons. For 4 odor associative learning experiments, we used: limonene, benzaldehyde, eugenol, and isoamyl acetate. For all associative or fear learning experiments, separate cohorts of mice were used.

2-photon imaging

2-photon imaging of the DG was performed using an Ultima IV laser scanning microscope (Bruker Nano, Middleton, WI) equipped with an 8Khz resonance galvanometer and high speed optics set, dual GaAsP PMTs (Hamamatsu model 7422PA-40), and motorized z focus (100nm step size). Approximately 30-90 mW of laser power (at 920nm, from MaiTai DeepSee mode-locked Ti:Sapphire laser source (Spectra-Physics, Irvine, CA)) was used during imaging, with adjustments in power levels to accommodate varying window clarity. Once a given power level was established for an animal, identical power was used across experiments to increase reliability in fluorescence detection across sessions. To optimize light transmission, we adjusted the angle of the mouse's head using two goniometers in the anterior-posterior and medial-lateral axis (Edmund Optics, +/−10 degree range) such that the GRIN lens was parallel to the objective. After focusing on the lens surface, optical viewing was switched to live view thru the 2-photon laser, and an FOV was located by moving the objective between ~50-300 microns upward. FOVs were chosen in the GCL, avoiding those FOVs where hilus was visible as previously shown (Danielson et al., 2016). Once an FOV was set for a given animal, each imaging session was manually aligned to approximate the same FOV across sessions. All images were acquired with a Nikon 20X NIR long working distance objective (0.45 NA, 8.3 mm WD). GCaMP6f signal was filtered through an ET-GFP (FITC/CY2) filter set. Acquisition speed was 30Hz for 512 × 512 pixel images. Images were averaged online for every 8 frames, yielding a final acquisition rate of 3.7 frames per second.

Appetitive Odor Conditioning

For the appetitive odor conditioning task, water-deprived mice were first habituated to the 2P setup with lick spout. Mice were given 50ul 10% sucrose by volume reward 100x (reward following regular intervals every 15 trials) for 3 days, or until mice successfully licked for reward < 1,000 times in under 10 minutes of head-fixation. After mice exhibited sufficient lick training, water-deprived mice were imaged under pseudorandom presentation of a three neutral odor panel, EB, MB, IAA (see above), with a 2 s trace delay followed by 50ms reward delivery window following each MB (odor b, CS+) trial (in order to isolate odor responses distinct from reward delivery), simultaneously with 2-photon imaging, and a variable ITI of 12-16 s. Reward was delivered regardless of whether the animal licked during odor b (CS+, MB) trials, and no punishment or time outs were administered if mice licked during the CS- trials. Mice were run once a day for 3 days through this task. All mice used in this study showed highly accurate licking to the CS+ odor by the 3rd day as analyzed by lick rates to the odor/trace period. Respiration was monitored using a Honeywell Airflow Sensor (AWM3300V). In the 4 odor task, mice were run in the same manner as above, but with 2 odors acting as the CS+, and 2 odors as the CS-. Separate cohorts of mice were run in either the 3 odor or 4 odor associative learning experiment. As with the 3 odor associative learning task, a total of 30 odor trials were delivered in pseudorandom order with a 4 s odor delivery period, 2 s trace, and 50ms reward window for two CS+ odors, followed by variable ITI between 12-16 s. The odorant identities of CS+ or CS- were randomly assigned for each mouse. Odorants used were: limonene, benzaldehyde, eugenol and isoamyl acetate. In this 4 odor associative learning task, mice were run for a 4th day of imaging, in which the lick spout was removed from the head-fixed setup to image mice in the absence of reward delivery.

Calcium data processing

Videos were motion corrected offline with the TurboReg registration plugin in FIJI. An average intensity z-projection of the first 100 stable frames (assessed manually) was used as a template with the translation model of motion correction. Cell segmentation and calcium transient time series data were extracted using Constrained Non-negative Matrix Factorization for microEndoscopic data (CNMF-E), a semi-automated algorithm optimized for GRIN lens Ca^{2+} imaging to denoise, deconvolve and demix calcium imaging data (Zhou et al., 2018). Briefly, this software uses a non-negative matrix factorization algorithm to extract the putative denoised calcium signals and spatial footprints. Putative neurons were identified, and sorted by visible inspection for appropriate spatial configuration and Ca^{2+} dynamics as described above, and putative units were manually merged or split from visual inspection. We ran the CNMF-E algorithm on each recording session separately to extract denoised calcium traces, inferred calcium events and spatial footprints. For all plots, we used the inferred calcium events for analysis unless otherwise specified.

Registration of cells across pre and post-conditioning sessions imaged at the same FOV was achieved using probabilistic modeling of similarities between cell pairs across sessions (Sheintuch et al., 2017). Briefly, spatial footprint maps were generated for each session by projecting the spatial filter of each cell onto a single image. Spatial footprint images from sessions imaged at the same FOV were then aligned. The distribution of similarities between pairs of neighboring cells were subsequently modeled via centroid distance to obtain an estimation for their probability of being the same cell (Psame). Cells were then registered across pre and post sessions via a clustering procedure that utilizes the previously obtained probabilities, with a probability threshold of 0.8. The average P_{same} value for registered cells was 0.96.

QUANTIFICATION AND STATISTICAL ANALYSIS

Odor responsivity

We defined cells as responsive to an odor by comparing the calcium events identified within all presentations of that odor with the events identified in the baseline period of 4 s preceding odor presentations. We used a two-sided Mann-Whitney-U test to assess if the difference in activity levels were statistically significant (**$p < 0.01$, *$p < 0.05$ for all tests in manuscript, see Table S1). Then, a cell was considered responsive if the FDR-adjusted p value of the statistical test was lower than 0.05 for a given odor or combination of odors (i.e., responsive to more than one odor). For raster plots of odor responses, normalized Ca event magnitude was generated by dividing each event magnitude by the mean event magnitude across the session and average across trial.

In learning experiments where we computed the stability of odor responses across sessions, we pooled all cells across all the mice and identified the same cells in the pre-(day 1) and post-conditioning (day 3) sessions through registration (see above). We considered cells that were responsive to one odor in the pre-conditioning session and their response profile in the post-conditioning session. We expressed the percentage of responsive cells in the post-conditioning session with respect to the subgroup of cells considered in the pre-conditioning session.

We also determined whether activity of LEC or DG neurons were modulated by reward consumption or correlated with licking or breathing. For reward responsivity, we generated peristimulus time histograms of normalized Ca^{2+} activity (by dividing the event magnitude by the mean event magnitude across the session) centered at the first lick after reward availability. Activity was averaged across trials (10) and cells for each mouse, and averaged across mice. Lick rates were computed in each time bin and averaged across trials and across mice.

To look for a relationship between licking or breathing and neural activity, we regressed the lick rates or the breathing rates across the session against the calcium events. We fit a linear regression model to predict lick rates or breathing rates and used the explained variance (r^2) as a measure of goodness of fit to compare the results across animals and days. We divided each analyzed session in 10

time-contiguous blocks and computed the generalization performance of the model with 10-fold cross-validation over these blocks to avoid overfitting. Regression was performed with regular linear regression with L2 norm or with Lasso, and verified that the results are not qualitatively different in either case (we report the more stringent case of Lasso in Figure S4).

Modulation index

For each odor presentation, we first extracted the raw calcium trace in a window between 5 s prior to the odor onset and 10 s after odor offset. We then divided all the traces by their standard deviation computed across all presentations of that odor as normalization. Finally, the modulation index was computed as:

$$\delta_f = \frac{r_s - r_b}{r_b} \times 100$$

where r_s is the mean calcium trace during odor presentation of a cell, averaged across trials, and r_b is the same quantity but computed on the 4 s preceding odor presentation.

Decoding

We used a linear decoder to discriminate patterns of activity into two discrete categories (Bishop, 2006):

$$y(t) = \theta(W\vec{r}(t) + b)$$

where $y(t)$ is the predicted label of the population activity pattern $\vec{r}$ recorded at time t and takes two values corresponding to the two classes of patterns to decode (for instance, the two odor identities), W is the vector of weights assigned to each cell and b is a constant bias term. Decoding parameters were obtained through a supervised learning protocol on labeled data using a support-vector machine (SVM) with a linear kernel (python/scikit/linearSVC). Data is reported as the generalized performance of the decoder using cross-validation, a standard machine learning procedure to avoid data overfitting. When multiple categories were involved, i.e., more than two odors, multiple linear decoders were trained on pairs of discrete categories combined using majority-based error-correction codes.

For decoding odor identity, we used a linear decoder trained on the recorded population activities. For each odor presentation, we defined the patterns of calcium activity by computing the mean event rates during the 4 s of odor presentation. We then evaluated the ability of the decoder to predict the odor identity based on the calcium activity on 10-fold cross-validated data, unless specified otherwise. To determine differences in the ability of our decoder to discriminate between single odor pairs, we used only the trials corresponding to that odor pair and measured performance in this subset with cross validation. For reporting decoding performance for single animals, we compared to a distribution of chance decoding performances computed by training our decoder on data in which odor identities were randomly shuffled with respect to the population activity patterns (n = 100 datapoints). When combining animals to compute average decoding performance of a group, we computed mean performance for each animal across different choices of training and test data (cross-validation) and performed a tests for significance from chance or between groups. When comparing decoding performance between neural populations of different size, we trained our decoder on a subsample of randomly chosen cells from the more numerous population equal to that of the smaller population. We repeated the operation 100 times and then combined the cross-validated decoding accuracies of all random choices together to get a single sample of decoding accuracies. In conditions where we pooled cells across animals, we generated pseudo-population recordings by combining cells across multiple FOVs. We generated 100 trials of pseudopopulation activity for each odor separately by choosing a random trial for each neuron independently. For decoding odor identity from the pseudopopulation, we divided the dataset in two halves. To generate the training set, we chose from trials of the first half, and for the test set, from the second half. To balance the number of cells across groups (for instance LEC vs DG) we also subsampled the cells by randomly selecting cells to generate the train and test patterns. We repeated the procedure 1000 times for statistical comparisons across groups and against chance decoding performance.

To decode odor identity around stimulus onset, we first averaged the event rates in 1 s long time bins between 3 s before odor presentation onset and 6 s after offset. We then trained a separate decoder for each time bin separately and assessed its performance on 5-fold cross-validated data.

For the DG model, we determined whether a model based upon random connectivity could generate the observed increase decoding performance in DG with respect to LEC. We first generated pseudopopulation data as explained above. We calibrated the sparsity in the model, i.e., the fraction of cells with a larger than zero calcium activity for any pattern, based on the training half of the pseudo-simultaneous population data. Then we equalized the number of cells across different groups to compare decoder performances by subsampling at random from the population of cells in a number equal to the minimum number of cells available across groups. We repeated the procedure to generate pseudo-population and cells subsampling 1000 times to perform statistical comparisons.

In the model, each LEC cell is connected through a synaptic matrix W to a fixed number of DG cells ($n = 10$) (Abusaad et al., 1999) with weights drawn from a Gaussian distribution of zero mean and unitary variance. DG cells are modeled as threshold-linear units, therefore the activity pattern in DG in the model $\vec{r}_{DG}$ is obtained from the activity pattern of LEC cells $\vec{r}_{LEC}$ as follows:

$$\vec{r}_{DG} = \theta(W\vec{r}_{LEC} - b)$$

where $\theta = 0$ if its argument is lower than zero and b is a threshold. The sparsity of activations in DG is regulated by the threshold b which is adjusted to match the sparsity levels across patterns of each odor in the DG data.

Ensemble similarity

To compute pattern similarities (McKenzie et al., 2016), we computed the mean event rates during each odor presentation in a session as well as the patterns during 4 s prior to odor onset as baseline. We then computed the mean cosine similarities (Pearson correlation) between every pair of patterns as:

$$s = \frac{1}{N}\sum_{i,j\neq i}^{N}\frac{\vec{r}_i\vec{r}_j}{|\vec{r}_i||\vec{r}_j|}$$

where $\vec{r}_i$ and $\vec{r}_j$ are the patterns of population activities for trial i and j and N is the total number of pairs of patterns counted once. The similarity values where then pooled to verify for statistical differences across categories of stimuli, for instance patterns of same odors versus patterns different odors, or patterns from the same session versus patterns from different sessions.

Overlaps

In order to compute overlapping responses, we determined the number of cells that showed statistically significant responses to two odors (or 3 odors for 3 odor overlap) (See Odor responsivity above). To assess statistical significance, we pooled together cells from all mice in each region to generate pseudo-simultaneous recordings. To generate chance distributions, we randomly assigned odor responses to all cells for each of the two odors (or 3 odors for 3 odor overlap) with probabilities that matched the proportion of responsive cells for each odor as in the real data. We computed the overlap for each random assignment and repeated the procedure 10000 times to obtain a chance distribution. We finally assessed the statistical significance of the actual overlap between the two (or 3) odors by computing the probability of obtaining that value from the chance distribution assuming a normal distribution of estimated mean and variance.

Lifetime sparseness

We computed lifetime sparseness by:

$$S = \frac{1 - A}{\left(1 - \frac{1}{N}\right)}$$

where N is number of odor stimuli and A is the activity fraction (Rolls and Tovee, 1995):

$$A = \frac{\left(\sum_i \frac{r_i}{N}\right)^2}{\sum_i \frac{r_i^2}{N}}$$

The activity fraction is computed on the average activity pattern r_i for each odor i (Vinje and Gallant, 2000):

$$r_i = \frac{1}{M}\sum_j r_i^j$$

where $j = 1, \ldots, M$ and M is the total number of trials.

Signal to noise (SNR)

We computed the Signal-to-Noise ratio by:

$$SNR = \frac{|S|^2}{|S - S_{raw}|^2}$$

Where S is the convolved calcium trace and S_{raw} is the raw calcium trace (Zhou et al., 2018).

Neuron, Volume *107*

Supplemental Information

The Dentate Gyrus Classifies Cortical Representations of Learned Stimuli

Nicholas I. Woods, Fabio Stefanini, Daniel L. Apodaca-Montano, Isabelle M.C. Tan, Jeremy S. Biane, and Mazen A. Kheirbek

Supplementary Figure 1

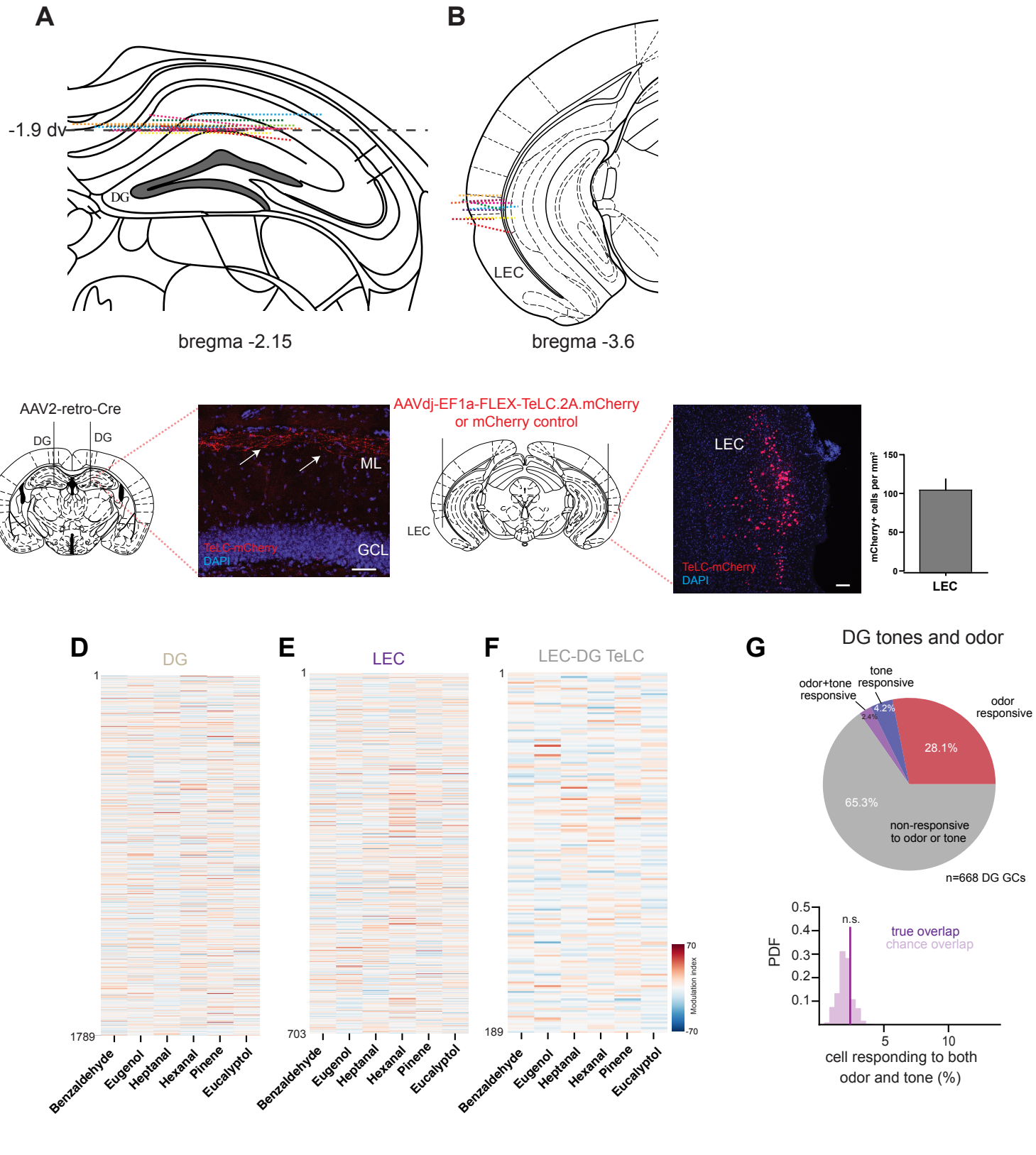

Supplementary figure 1 (Related to Figures 1-5)
A-B. Reconstructed lens implant locations of total of DG (A) and LEC mice (B) used throughout study, with dotted line indicating the estimated location of the impression left by lens on tissue, superimposed on mouse brain atlas. **C.** LEC-DG TeLC based synaptic silencing, with mCherry positive terminals shown within the outer molecular layer shown on left (arrowheads), and a representative coronal section showing mCherry positive cells located in LEC on right, with mCherry positive cells quantified across animals used throughout study (mean +/- SEM, n=11 mice). Scale bars: 100 microns. **D-F.** Odors elicit distributed responses in the population of recorded DG GCs. Modulation index (see Methods) for each cell (in rows) combined across n = 8 DG mice (D), n=7 LEC mice (E) and n= 3 LEC-DG TeLC mice (F) is color coded for the panel of six neutral odors (in columns). Same 6 neutral odors as labeled in Figure 1. **G.** Cells co-responsive to tones and odors are not more prevalent than expected by shuffling odor and tone responses across cells. Mice were presented 3 neutral odors and 3 tones (see Methods). Odor responsive and tone responsive overlap cells (pie chart, above) are compared to a chance overlap distribution obtained by pooling cells from all mice. Pie chart shows percentage of only tone, only odor, tone+odor co-responsive cells, or non-responsive cells. Odor responsive and tone responsive overlap cells are compared to a chance overlap distribution (n=668 cells in 3 mice, $p>0.05$). Error bars represent SEM. For exact *P* values, see Supplementary Table 1.

Supplementary Figure 2

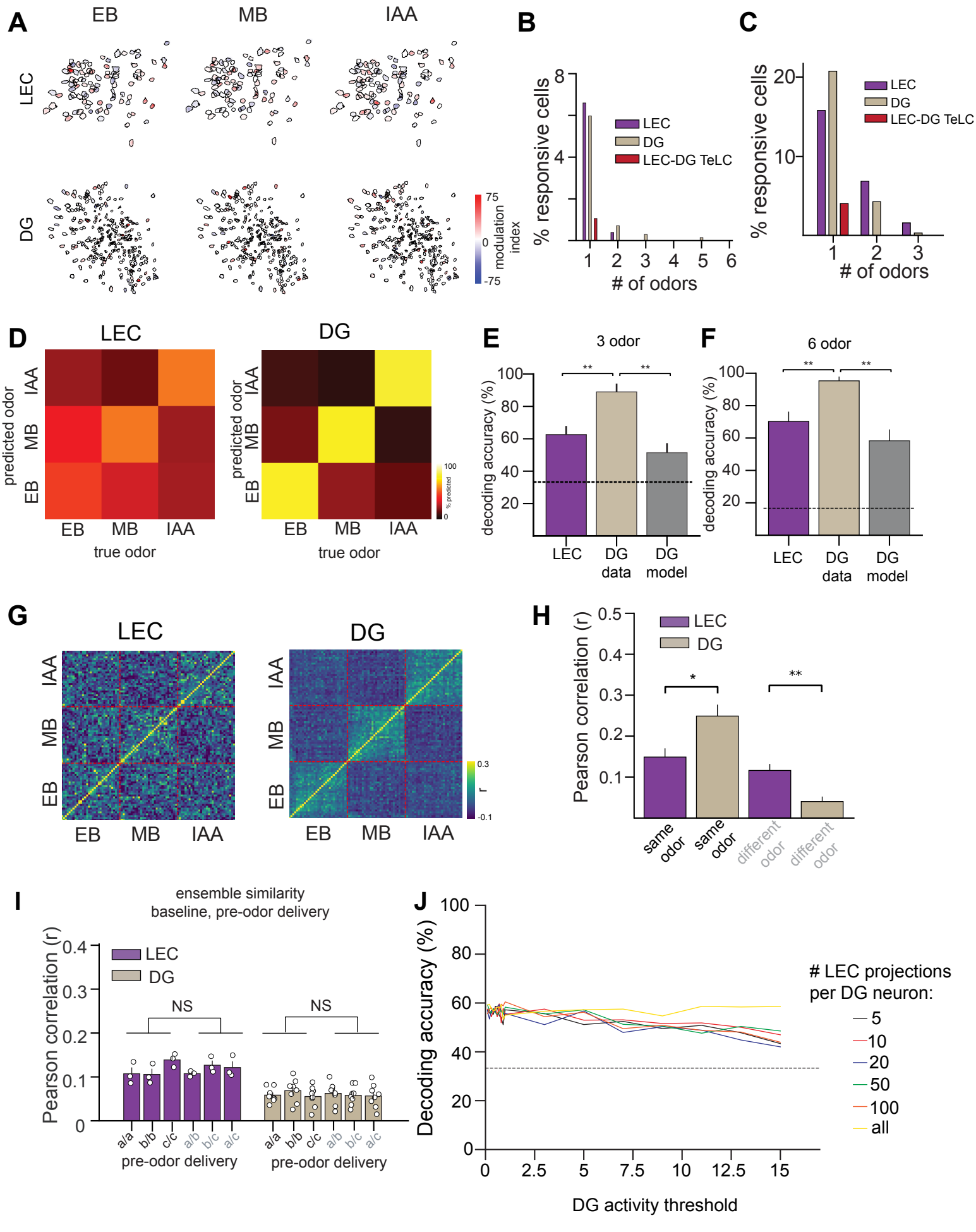

Supplementary figure 2 (related to figure 4)

A. Odor responses to EB/MB/IAA are sparse and randomly distributed in the FOV. Spatial footprints shown from an example mouse, with overlaid modulation index for each cell (see Methods). **B.** Percent responsive cells in 6 odor (benzaldehyde, eugenol, heptanal, hexanal, pinene, eucalyptol) experiment in DG, LEC and LEC-DG TeLC mice. **C.** Percent responsive cells in 3 odor experiment (ethyl butyrate, methyl butyrate, isoamyl acetate) in DG, LEC and LEC-DG TeLC mice. **D**. Confusion matrices for decoding accuracy in the three odor experiment in DG and LEC. G-H**. E-F.** The accuracy of a decoder to classify odor identity was greater in DG than in LEC activity for both the 3 odor (E) and 6 odor (F) experiment. A model of DG based on random connectivity with comparable levels of sparseness could not perform as well as real DG data in classifying odor identity in either the 3 odor or 6 odor design . (linear SVM classifier with matched number of cells in DG and LEC, 3 odor: n=190 cells (n-matched, from 3 LEC and 8DG mice), 6 odor n=703 cells, (n-matched, from 3 LEC and 8DG mice), t-test, **p<0.01). **G.** Trial by trial similarity matrix in DG and LEC mice for the three odor experiment. **H**. Odor ensembles were more distinct for presentation of different odorants in DG than LEC mice, and in this experiment, within odor correlations were higher in DG compared to LEC mice. (Pearson correlation of activity vectors during odor presentation, n= 8 DG mice, 3 LEC mice, Mann-Whitney, **p<0.01, * p<0.05). **I**. Ensemble similarities computed in non-odor delivery baseline periods. **J**. Decoding accuracy in the DG GCs model doesn't depend on sparsity. We varied the proportion of LEC projections per DG GCs as well as the activation threshold for each model neuron. The parameters effectively change the sparsity of activations across neurons in DG and are the only parameters in the model. For each pair of parameters, we ran 10 models and report here the average decoding accuracy across models. Error bars represent SEM. For exact *P* values, see Supplementary Table 1.

Supplementary Figure 3

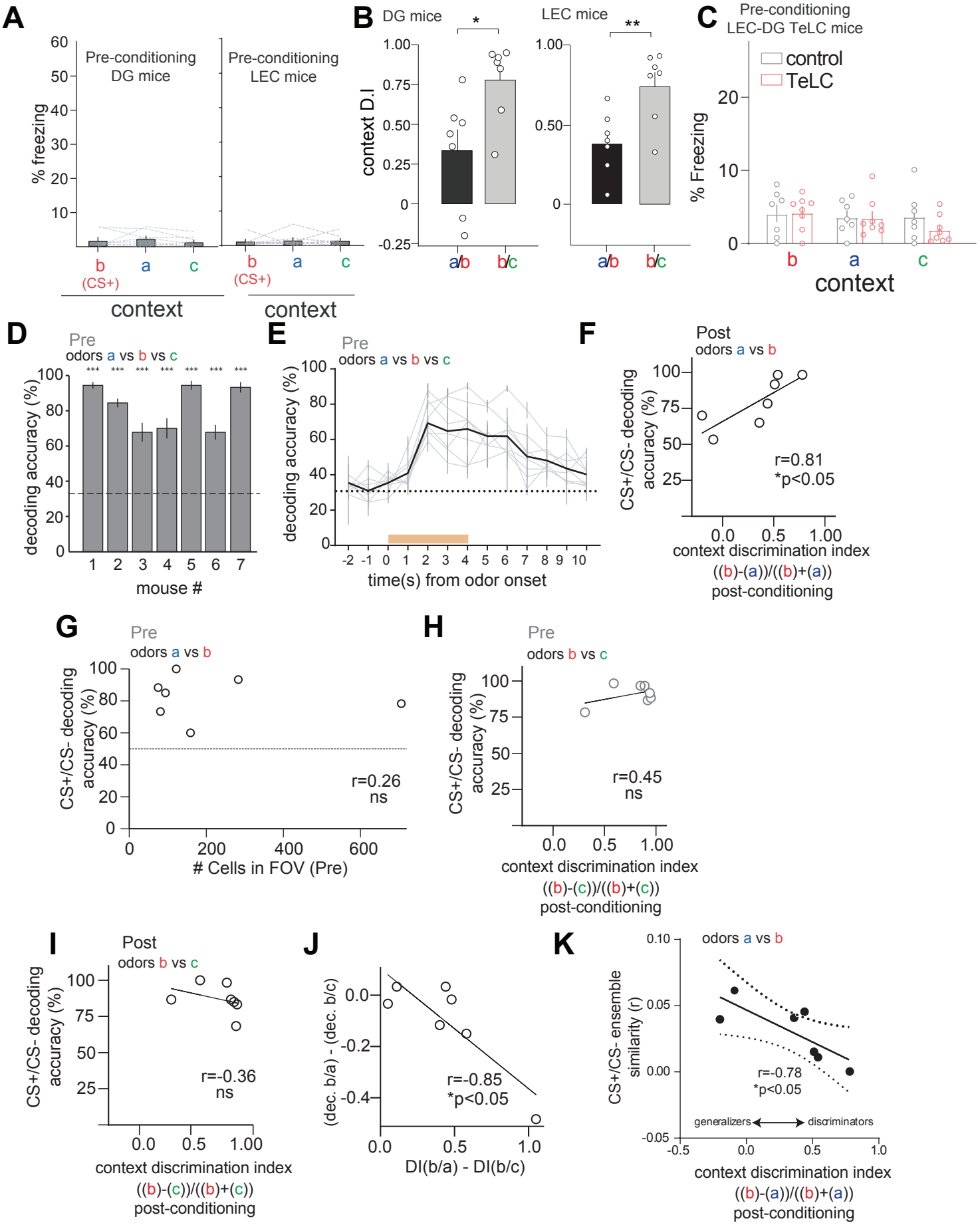

Supplementary figure 3 (related to Figure 4)
A. Left DG mice, right, LEC mice. Pre-conditioning percent time spent freezing to each context, showing lack of initial fear responses to neutral odorants (one-way ANOVA, $p>0.05$). **B.** Left DG mice, right, LEC mice. Context discrimination indices comparing a/b contexts and b/c contexts. In both the DG and LEC cohorts, mice were better at discriminating distinct context pairs (b/c) compared to context pairs (a/b) (n=7 mice/group, t-test , $p<0.05$). **C.** Preconditioning context discrimination did not differ between control and LEC-DG TeLC mice. **D.** Baseline, pre-learning odor identity could be decoded in all mice tested (3 odor decoding, SVM with linear kernel, one sample t-test, $p<0.001$ for all mice from chance decoding performance (see Methods for single animal decoding), error bars indicate SEM from cross validation of decoder). **E.** Odor identity could be decoded within 2s of odor onset (n=7 mice, all values mean +/- SEM for each mouse). For each 1s timebin, a different decoder is trained on the data for the corresponding bin. Generalization performance on held-out data is reported as decoding accuracy. The solid black line corresponds to mean across mice in each time bin. For all mice, the decoding performance was significantly higher than chance (dashed line) for several seconds after odor offset. **F.** Decoding accuracy of odor a vs odor b in the post-conditioning session correlated with context freezing behavior (Pearson $r=0.81$, $p<0.05$, n=7 mice). **G.** Decoding performance for a/b does not depend on number of cells per mouse (Pearson $r=0.26$, $p>0.05$, n=7 mice). **H-I.** Decoding accuracy of odors b and c (MB and IAA) before or after fear learning does not correlate with freezing behavior after learning (pre $r=0.45$, post $r=-0.36$, n=7 mice, linear fit with solid line, $p>0.05$, n=7 mice). **J.** Better discriminability of contexts a/b vs b/c correlate with decoding of these odors. (Pearson $r=-0.85$, $p<0.05$, n=7 mice). **K.** Pearson similarity ensemble metric was generated for odors from contexts a/b and plotted against pre-conditioning context discrimination index for contexts a/b. (Pearson $r=-0.78$ and $p<0.05$, n=7 mice). Error bars represent SEM. For exact *P* values, see Supplementary Table 1.

Supplementary Figure 4

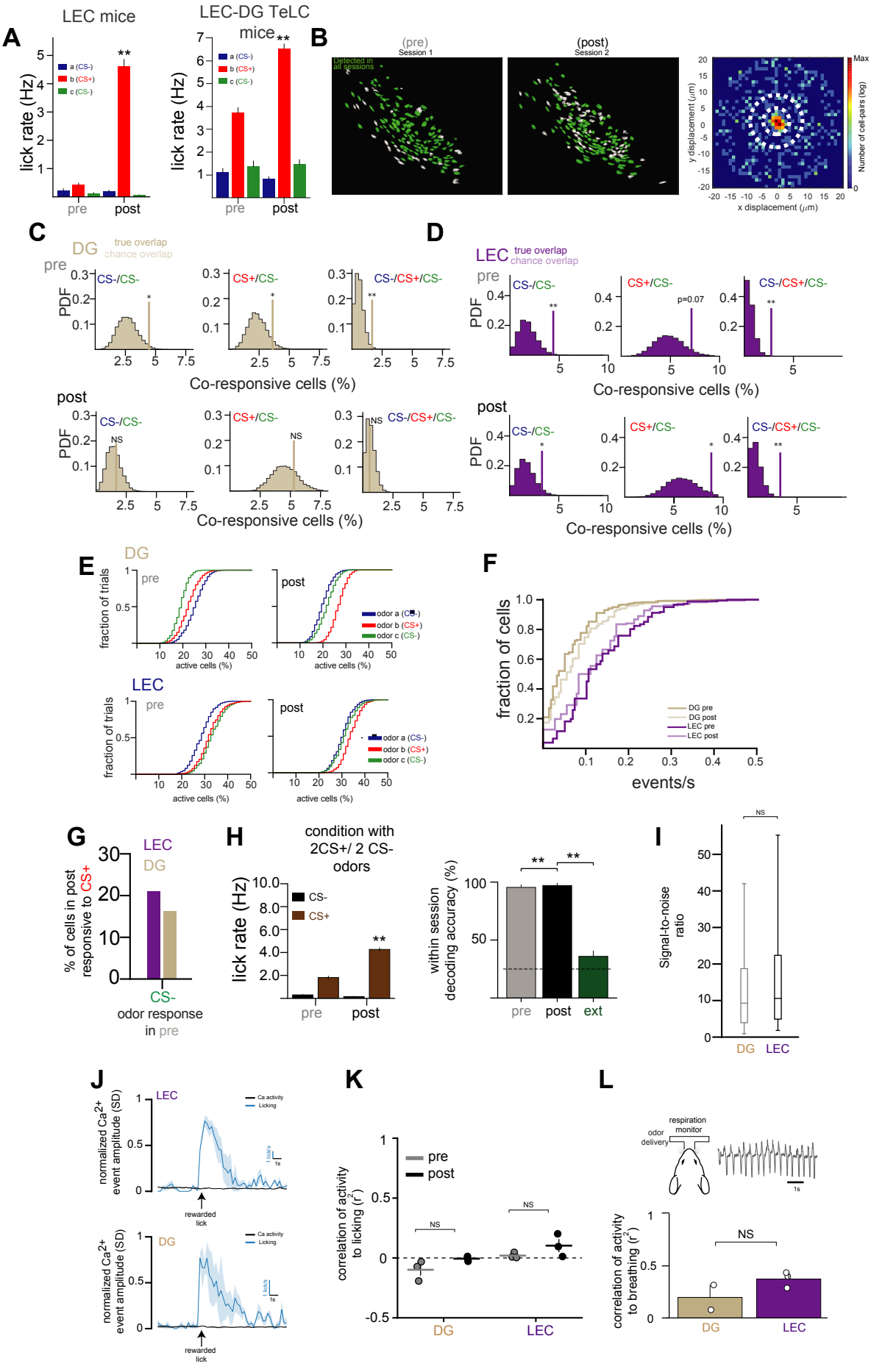

Supplementary Figure 4 (related to Figure 5)

A. Average lick rates during the odor and trace period on day 1 (pre) and day 3 (post) in LEC mice, and in LEC-DG TeLC mice, as analyzed in Figure 4 (Mann-Whitney, **p<0.001) **B.** Example pre and post spatial footprints showing registration results of identified ROIs that are within centroid differences established within 95% of a confidence interval. Average centroid displacement shown on right for registering cells pre to post, using *CellReg* algorithm. **C-D.** Overlaps of cell responses for odor pairs and triples before and after learning for all recorded DG GCs (C), and LEC cells (D), (level of significance for 10,000 shufflings, , **p<0.01, *p<0.05, n=3 DG mice and n=3 LEC mice). **E.** Fraction of trials that cells are active, plotted for each individual odor in DG and LEC. After learning, an increased percentage of cells are responsive to the CS+ odor across trials within DG. (DG post, CS+ odor vs all others KS test, P<0.001). **F.** Cumulative distribution plot arranged by calcium event rate pre and post learning (average events per second for each cell during entire imaging period, KS test, p<0.001 between LEC and DG). **G.** Odor responses in Post for cross-session registered cells. Cells were classified as CS- (IAA) responsive Pre, and then their responses were determined in Post. Unlike with the EB/MB pair in Figure 5K,a similar proportion of LEC and DG neurons became responsive to the CS+ odor after learning. (n=3 DG mice, 359 cells; n=3 LEC mice, 182 cells X2 test, p<0.01). **H**. Four odor associative learning task. Four distinct odors were given, and two CS+ odors were followed by a trace period and a sucrose reward (CS+ assignment randomized among mice). *Left*, lick rate to CS+ odors in pre and post learning.(n=2 mice, **p>0.01) Mice show CS+ biased licking on the first day in this design. Proportion of CS+ responding cells in the DG increase after learning (n=2 mice p<0.01) *Right.* High decoding accuracy on D1 with improvement with learning. Decoding accuracy was reduced in an extinction session with the lick spout removed (n=443 cells, from 2 DG mice, **p<0.01). **I.** Signal-to-noise (SNR) for all cells combined across LEC (n=360 in 3 mice) and DG mice (n=531 in 3 mice). The horizontal line represents the median SNR for each population, the boxes represent first and thirds quartile of the distribution and the whiskers represent 9th and 95th percentiles. The two distributions are not significantly different (t-test, p=0.87). **J.** A cohort of DG and LEC mice were imaged for sucrose responses in the absence of odor delivery. For all cells we calculated a peri-stimulus time histogram (PSTH) for normalized Ca^{2+} activity (black line) triggered on the first lick after sucrose availability (licking rate in blue). Reward consumption did not modulate DG (531 cells in 3 mice) or LEC (n=360 cells in 3 mice) activity. Shaded areas are +/-SEM. **K-L.** Linear regression of lick rates (K) and breathing rates (L) and Ca^{2+} in DG and LEC before (pre) and after (post) associative learning (see Methods). We found that neural activity is not significantly correlated to lick rates (R^2 is approximately zero for all animals in both sessions, DG pre n=531 cells in 3 mice, DG post n=627 cells in 3 mice, LEC pre n=360 cells in 3 mice, LEC post n=266 cells in 3 mice, no significant difference between pre and post in either group, p>0.05). In addition, we found that correlations of breathing rates with Ca^{2+} did not differ between LEC and DG recordings (n=2 LEC mice, 3 DG mice, Mann Whitney, p>0.05). All error bars represent mean +/- SEM. For exact *P* values, see Supplementary Table 1.

figure	unit of comparison	variable	n	test	results (p-value)
Fig. 3c	pseudopopulation of cells, 10000 iterations (see methods)	6 odor decoding accuracy	dg=8, lec=7, tent=3, 189 cells, n matched	mann whitney U	LEC vs DG p<0.0001, DG vs LEC-DG TeLC p<0.0001
Fig. 3e	cells from trial pairs	lec same, lec diff	42, 105 (from 7 LEC mice)	t-test for independence	t=5.69, p=6.5E-08
		lec same, dg same	42, 48 (8 DG and 7 LEC mice)		t=-.071, p=0.483
		dg same, dg diff	48, 120 (8 DG mice)		t=-7.81, p=0.6.28E-13
		lec diff, dg diff	105, 120 (8 DG and 7 LEC mice)		t=-2.556, p=0.01
		TeLC same, TeLC diff	18, 45 (3 LEC-DG TeLC mice)		t=-1.65, p=0.104
Fig.4a	mice	percent time spent freezing to each odor	8 TeLC, 7 control	repeated measures ANOVA	odorXgeno interaction F = 6.16 and p<0.0001
				Holm-Sidak's multiple comparison	odor eb(a), p=0.303 odor mb(b), p<0.001 odor iaa (c), p=0.755
Fig 4c	mice	percent time spent freezing to each odor	7DG	one-way ANOVA	ANOVA summary: F=37.6, p<0.001
				Holm-Sidak's multiple comparison	odors mb (b) vs. eb (a), p=0.007 odors mb (b) vs. iaa (c), p=<0.001 odors eb (a) vs. iaa (c), p=0.005
Fig. 4d	mice	discrimination index of (a/b) vs. PRE-conditionig decoding performance (a/b)	7 DG	pearson correlation coefficient	r=0.959, p=0.0003
Fig 4e	mice	percent time spent freezing to each odor	7LEC	one-way ANOVA	ANOVA summary: F=30.26, p<0.001
				Holm-Sidak's multiple comparison	dors mb (b) vs. eb (a), p<0.001 odors mb (b) vs. iaa (c), p<0.001 odors eb (a) vs. iaa (c), p=0.006
Fig. 4f	mice	discrimination index of (a/b) vs. PRE-conditionig decoding performance (a/b)	7 DG	pearson correlation coefficient	r=-0.2406, p=0.3016
Fig. 5c	animals	lick rate (Hz) during 2s delay vs. baseline	3 DG	Mann-Whitney	U=1187.5, p=8.62e-18
Fig. 5f	cells	co-responsive odor a/b cells vs. chance overlap PRE and POST learning	359 (3 DG mice)	p-value relative to shuffle (10,000)	PRE: EB/MB (a/b): p=0.0044 POST: EB/MB (a/b): p=0.312
Fig. 5g	cells	co-responsive odor a/b cells vs. chance overlap PRE and POST learning	182 (3 LEC mice)	p-value relative to shuffle (10,000)	PRE: EB/MB (a/b): p=0.00413 POST: EB/MB (a/b): p=0.0129
Fig. 5h	cells	fraction total cells active for all odors PRE vs. POST learning	359 (3 DG mice)	t-test for independence, bonferroni correction for n=6	EB (a): p= 3.970e-05 MB (b): p=4.688e-04
Fig. 5i	cells	fraction total cells active for all odors PRE vs. POST learning	182 (3 LEC mice)	t-test for independence, bonferroni correction for n=6	EB (a): p=5.49e-01 MB (b): p=1.00
Fig. 5j	cells	fraction total cells active for all odors PRE vs. POST learning	150 cells (2 LEC-DG TeLC mice)	t-test for independence	EB (a): t=-4.222 p=4.78E-05 MB (b): t=-6.176 p=9.63E-09
Fig. 5K	cells	fraction of responsive cells in POST among responsive cells in PRE for each odor	182 LEC and 359 DG, PRE and POST learning	Chi-square, Bonferroni adjusted	EB (odor a, CS-) chi=56.0, p=9.4439e-10, p_adj=2.8332e-09 MB (odor b, CS+) chi=14.0, p=5.1181e-02, p_adj=1.5354e-01 IAA (odor c) chi=16.0, p=2.5116e-02, p_adj=7.5349e-02
Fig. 5l	mice	lifetime sparsity PRE vs. POST	3 DG	Mann-Whitney	U=1.45e+05, p=1.317e-03
	mice	lifetime sparsity PRE vs. POST	3 LEC	Mann-Whitney	U=4.36e+04, p=5.699e-02
Fig. 5m	mice	3 odor (a/b/c) decoding accuracy PRE vs. POST	n= 359 cells from 3 DG mice	Mann-Whitney	U=264.00, p=4.692e-03
	mice	3 odor (a/b/c) decoding accuracy pre vs. post	n=182 cells from 3 LEC mice	Mann-Whitney	U=282.00, p=1.1632e-02

	mice	3 odor (a/b/c) decoding accuracy pre vs. post	n=150 cells from 2 mice	Mann-Whitney	U=161.5, p=0.296
Fig. 5n	mice	across session decoding accuracy (3 odors (a/b/c))	3 DG and 3 LEC mice	Mann-Whitney	U= 2.28e03, p=1.082e-12
supplementary figures					
Fig. S1g	cells	odor and tone co-responsive cells vs. chance overlap	668 (3 DG mice)	p-value relative to shuffle (10,000)	p = 0.238
Fig S2e	n matched cells, 1000 iterations (see methods)	3 odor (a/b/c) decoding accuracy in LEC vs. DG vs. DG model	190 LEC vs. 190 DG (n-matched) n=3LEC, 8DG	t-test	LEC vs. DG: t=-25.04, p=2.22e-44
					DG vs. model: t=34.31, p=2.43e-72
Fig S2f	n matched cells, 1000 iterations (see methods)	6 odor (a/b/c) decoding accuracy in LEC vs. DG vs. DG model	703 LEC vs. 703 DG (n-matched) from 8 DG mice, 7 LEC mice	t-test	LEC vs. DG: t=-118, p<0.0001 DG vs. model: t=226, p<0.0001
Fig S2h	cells from trial pairs	lec same, dg same	(8 DG and 3 LEC mice)	t-test for independence	t=-2.09, p=0.04
		lec diff, dg diff	(8 DG and 3 LEC mice)		t=3.41, p=0.002
Fig. S2i	animals	Pearson correlation grouped for same odor vs. different odor	LEC 3	Mann-Whitney	U=38.00, p=0.859
			DG 8	Mann-Whitney	U=303.00, p=0.765
Fig. S3a	mice	percent time spent freezing to each odor	7 DG	one-way ANOVA Holm-Sidak's multiple comparison	ANOVA summary: F=0.5320, p=0.538 odors mb (b) vs. eb (a), p=0.851 odors mb (b) vs. iaa (c), p=0.851 odors eb (a) vs. iaa (c), p=0.330
			7 LEC	one-way ANOVA Holm-Sidak's multiple comparison	ANOVA summary: F=0.05242, p=0.937 odors mb (b) vs. eb (a), p=0.991 odors mb (b) vs. iaa (c), p=0.991 odors eb (a) vs. iaa (c), p=>0.999
Fig. S3b	mice	(a/b) discrimination index vs. (b/c) discrimination index	7 DG	t-test	t=-2.78, p=0.0167
Fig. S3b	mice	(a/b) discrimination index vs. (b/c) discrimination index	7 LEC	t-test	t=-3.188, p=0.0078
Fig. S3c	mice	percent time spent freezing to each odor	8 TeLC, 7 control	one-way ANOVA Holm-Sidak's multiple comparison	ANOVA summary: F=2.335, p=0.148 odors mb (b) vs. eb (a), p=0.560 odors mb (b) vs. iaa (c), p=0.06 odors eb (a) vs. iaa (c), p=0.424
Fig. S3d	mice	3 odor (a/b/c) PRE-conditioning decoding score	7 DG	t-test	p<0.0001 for all individual mice comparisons to chance
Fig. S3f	mice	discrimination index of (a/b) vs. POST-conditioning decoding performance (a/b)	7 DG	pearson correlation coefficient	r = 0.81, p = 0.0273
Fig. S3g	mice	number of cells per FOV vs. PRE-conditioning decoding accuracy (a/b)	7 DG	pearson correlation coefficient	r=0.26, p=0.579
Fig. S3h	mice	discrimination index of (b/c) vs. PRE-conditionig decoding performance (b/c)	7 DG	pearson correlation coefficient	r = 0.45, p = 0.312
Fig. S3i	mice	discrimination index of (b/c) vs. POST-conditionig decoding performance (b/c)	7 DG	pearson correlation coefficient	r = -0.36, p = 0.4298
Fig. S3j	mice	discrimination index difference (b/a-b/c) vs. decoding difference (b/a-b/c)	7 DG	pearson correlation coefficient	r=-0.85, p=0.014

Fig. S3k	mice	discrimination index of (a/b) vs. pre-conditionig ensemble pearson similarity metric (a/b)	7 DG	pearson correlation coefficient	r=-0.78, p=0.02
Fig. S4a	mice	lick rate (Hz) during 2s delay vs. baseline	3 LEC	Mann-Whitney	U=285.00 , p=2.095e-28
Fig. S4a	mice	lick rate (Hz) during 2s delay vs. baseline	2 LEC-DG TeLC	Mann-Whitney	U=514.0 , p=6.634e-12
Fig. S4c	cells	co-responsive odor cells vs. chance overlap PRE and POST learning	359 (3 DG mice)	p-value relative to shuffle (10,000)	PRE: EB/IAA (a/c): p=0.0115 PRE: MB/IAA (b/c): p=0.0395 PRE: MB/EB/IAA (a/b/c): p=0.000494 POST: EB/IAA (a/c): p=0.0223 POST: MB/IAA (b/c): p=0.0448 POST: EB/MB/IAA (a/b/c): p=1.39E-06
Fig. S4d	cells	co-responsive odor cells vs. chance overlap PRE and POST learning	182 (3 LEC mice)	p-value relative to shuffle (10,000)	PRE: EB/IAA (a/c): p=0.001367 PRE: MB/IAA (b/c): p=0.0710 PRE: MB/EB/IAA (a/b/c): p=6.36E-08 POST: EB/IAA (a/c): p=0.0223 POST: MB/IAA (b/c): p=0.0448 POST: EB/MB/IAA (a/b/c): p=1.39E-06
Fig. S4e	cells	cumulative distribution function of percent active cells vs. number of trials active, PRE and POST learning for odors a, b, c	182 LEC and 359 DG, PRE and POST learning	parametric t-test for independence, Bonferroni adjusted for n=12	LEC PRE: EB/MB (a/b): t=-3.11, p=2.87e-03 EB/IAA (a/c): t=-3.83, p=3.12e-04 MB/IAA (b/c): t=-0.654, p=5.15e-01 LEC POST: EB/MB (a/b): t=-3.58, p=6.911e-04 EB/IAA (a/c): t=-3.58, p=7.21e-01 MB/IAA (b/c): t=3.06, p=3.32e-03 DG PRE: EB/MB (a/b): t=2.60, p=1.156e-02 EB/IAA (a/c): t=6.03, p=1.184e-07 MB/IAA (b/c): t=3.31, p=1.57e-03 DG POST: EB/MB (a/b): t=-8.83, p=2.45e-12 EB/IAA (a/c): t=-2.50, p=1.49e-02 MB/IAA (b/c): t=6.18, p=6.79e-08
Fig. S4f	cells	cumulative distribution function for event rate, PRE vs. POST learning for LEC and DG	182 LEC and 359 DG, PRE and POST learning	KS 2-samples	LEC p = 0.0124, DG p = 0.00002554, LEC adjusted Bonf. p = 0.02482, DG adjusted Bonf. P<0.001
Fig. S4g	cells	fraction of responsive cells in POST among responsive cells in PRE for each odor	182 LEC and 359 DG, PRE and POST learning	Chi-square, Bonferroni adjusted	IAA (odor c, CS-) chi=16.0, p=2.5116e-02, p_adj=7.5349e-02
Fig. S4h	mice	lick rate (Hz) during 2s delay vs. baseline	2 mice	Mann-Whitney	pre vs post U=10648.0, p<0.001
Fig. S4h	1000 iterations (see methods)	4 odor decoding accuracy	n=443 cells from 2 DG mice	Mann-Whitney	pre vs post U=2.68e+03, p=1.488e-08, post vs ext U=1.00e+04, p=2.455e-34
Fig S4i	cells	SNR	n= 3 DG mice (531 cells), 3 LEC mice (360 cells)	t-test	t=-0.160, p=0.87
Fig S4k	mice	correlation to licking (pre vs post)	N=3 LEC, 3 DG	Mann-Whitney	DG U=0.0, p=0.08, LEC U=1.0, p=0.19
Fig S4l	mice	correlation to breathing (LEC vs DG)	N=2 LEC, 3 DG	Mann-Whitney	U=5.0, p=0.386

Supplementary Table 1 (related to all Figures). Summary of statistics in all figure panels in manuscript.